

# Earth and Space Science



## RESEARCH ARTICLE

10.1029/2021EA001703

### Key Points:

- A rock magnetic and anisotropy of magnetic susceptibility study was conducted on the subglacial Itararé Group sedimentary rocks of Brazil
- Rock-magnetic evidence reveals a complex magnetic mineralogy and allows determining a dominantly paramagnetic origin for the AMS
- AMS analyses determine a dominant sedimentary transport direction to the NW and allow determining the depositional regimes for these rocks

### Supporting Information:

Supporting Information may be found in the online version of this article.

### Correspondence to:

D. Bilardello,  
[dario.bilardello@gmail.com](mailto:dario.bilardello@gmail.com)

### Citation:

Bilardello, D. (2021). Late Paleozoic depositional environments and sediment transport directions of the Itararé Group rocks from the state of São Paulo, Brazil, determined from rock magnetism and magnetic anisotropy. *Earth and Space Science*, 8, e2021EA001703. <https://doi.org/10.1029/2021EA001703>

Received 18 FEB 2021

Accepted 27 APR 2021

## Late Paleozoic Depositional Environments and Sediment Transport Directions of the Itararé Group Rocks From the State of São Paulo, Brazil, Determined From Rock Magnetism and Magnetic Anisotropy

Dario Bilardello<sup>1</sup> 

<sup>1</sup>Institute for Rock Magnetism, University of Minnesota, Minneapolis, MN, USA

**Abstract** Sedimentary rocks of the Itararé Group, deposited during the Late Paleozoic Ice Age in the Paraná Basin of South America, were collected throughout the state of São Paulo, Brazil, for an anisotropy of magnetic susceptibility (AMS) and rock-magnetic study. A recent paleomagnetic study conducted on the same samples had determined that these rocks were largely remagnetized during the Cretaceous; however, rock-magnetic experiments demonstrate that the AMS is dominantly carried by paramagnetic minerals and therefore is unaffected by the secondary magnetic overprints. AMS data are analyzed in terms of their shape and orientation, and according to the relationship between the  $q$ -value (magnetic lineation/foliation) and the imbrication angle ( $\beta$ ) of the minimum susceptibility axes with respect to bedding ( $q$ - $\beta$  diagram). Using multiple lines of evidence, we demonstrate that AMS records primary sedimentary fabrics that reflect the depositional environments and paleocurrent conditions in which these rocks were deposited. The magnetic fabrics consistently record a SE-NW paleocurrent orientation, with dominant direction of transport to the NW throughout the entire state of São Paulo, in agreement with ice flow and sediment transport directions reported from limited numbers of sites possessing sedimentary structures and ice-kinematic indicators.

## 1. Introduction

During the Late Paleozoic, the supercontinent Gondwana was positioned over the South Pole and was affected by one of the most significant glaciations in Earth's history. Sedimentary records of this Late Paleozoic Ice Age (LPIA) are widespread across the mid-latitude to high-latitude sedimentary basins of Gondwana (e.g., da Rosa et al., 2016; Fedorchuk et al., 2019; Isbell et al., 2003; Rosa et al., 2019; Santos et al., 1996; Scotese et al., 1999).

The Paraná Basin is the largest of the Late Paleozoic intraplate basins in South America: roughly NNE-SSW elongated, it comprises a widespread sedimentary-magmatic sequence that is up to ca. 7,000 m in thickness, containing one of the most extensive LPIA records. Glacial deposits are found within the Permo-Carboniferous Itararé Group, which constitutes one of the largest units within the basin (França & Potter, 1988; Rocha-Campos et al., 2008; Santos et al., 1996). The Itararé Group was deposited under mostly marine glacial and periglacial conditions, comprising several sedimentary facies. The Group is subdivided into the Lagoa Azul, Campo Mourão, and Taciba Formations (e.g., França & Potter, 1988) and represents glacial-subglacial successions with transgressive shales at the top of each sequence, interpreted as sea-level rise during glacial melting. Lithologies of each formation comprise diamictites, sandstones, siltstones, shales, and conglomerates (França & Potter, 1988, 1991; Limarino & Spalletti, 2006; Rocha-Campos et al., 2008; Santos et al., 1996). In the northern part of the basin, true subglacial tillite deposition is rare (Arab et al., 2009), with the majority of the sandy deposits pertaining to proximal glacial-marine environments, and interpreted as subaqueous outwash-fan apron deposits, grading laterally into diamictites and mudstones (Carvalho & Vesely, 2017; França & Vesely, 2007; Mottin et al., 2018). Mass transport of resedimented sediment results in massive diamictites, often developing into gravitational flows and occasional turbidites (França & Vesely, 2007; Vesely et al., 2018). More distally, the sedimentation evolves to tractional flows plus suspension fall-out of the abundant rhythmite sequences and to the shale deposits resulting from pure suspension (França & Vesely, 2007; Vesely et al., 2018).

© 2021. The Authors.

This is an open access article under the terms of the [Creative Commons Attribution-NonCommercial License](https://creativecommons.org/licenses/by-nc/4.0/), which permits use, distribution and reproduction in any medium, provided the original work is properly cited and is not used for commercial purposes.

The correlation between outcrops and subsurface sections is not fully established (Rocha-Campos et al., 2008) and unlike the southern portion of the basin, there is no lateral continuity of the Itararé Group sedimentary facies to the north, particularly in the thick sequence within the state of São Paulo, hindering the establishment of formal stratigraphic subunits and correlations (Arab et al., 2009). Furthermore, in the northern part of the Paraná Basin, the Itararé Group assumes a red coloration and is referred to as the Aquidauana Formation, however, the two are equivalent (Gesicki et al., 1998, 2002; Milani et al., 1994, 1998). Igneous rocks (lava flows, dykes, and sills) within the Itararé Group are not uncommon and are related to Triassic–Jurassic and the Early Cretaceous magmatic events associated with the opening of the South Atlantic (e.g., Abbott & Isley, 2002; C. C. Araújo et al., 2005; L. M. Araújo et al., 2000; Ernesto et al., 1999; Menezes & Travassos, 2000; Milani & Zalán, 1999; Thomaz Filho et al., 2008) and are responsible for the remagnetization of the Itararé Group rocks (Bilardello et al., 2018).

Absolute U–Pb ages for the Itararé Group sedimentary rocks of 298.5 ( $\pm 2.6$ ) and  $\sim 323$  Ma from the lower Itararé Group were reported by Franco et al. (2012). The latter age is derived from a detrital zircon and represents an Upper Mississippian age limit. An U–Pb age of 267.1 ( $\pm 3.4$ ) from the overlying Rio Bonito Formation instead represents an age limit for the upper portion of the Itararé Group (Matos et al., 2001). According to Souza (2006), the oldest palynozone in the basal portion of the Itararé Group is Late Bashkirian ( $\sim 315$ – $312$  Ma), and Holz et al. (2010) also reported the Itararé as Bashkirian/Moscovian ( $\sim 312$  Ma) to Early Sakmarian ( $\sim 294$  Ma). The palynological ages thus place the base of the Itararé as Early Pennsylvanian, whereas the absolute U–Pb ages could push the base into the Late Mississippian. The Late Carboniferous age of the Itararé is further supported by palynological correlation with Late Carboniferous strata in Argentina, Africa, and Australia (Holz et al., 2010), as well as the U–Pb ages of 302.0–299.2 Ma from the African Karoo Supergroup (Bangert et al., 1999).

Structures associated with the LPIA glaciation occur throughout the Paraná Basin, with ice dynamics primarily determined through striations and grooves on basement rocks (e.g., da Rosa et al., 2016; Gesicki et al., 2002; Rosa et al., 2019). Within the Itararé Group deposits, glacier kinematics have been inferred indirectly from paleocurrent trends in ice-distal facies (e.g., Arab et al., 2009; Carvalho & Vesely, 2017; da Rosa et al., 2016; Mottin et al., 2018) and directly from subglacial deformational structures (e.g., da Rosa et al., 2016; Gesicki et al., 2002; Rocha-Campos et al., 2000). Specific to the state of São Paulo, scarce direct evidence derived from landforms and striations arising from glacier movement at eight different sites consistently indicates ice-flow direction to the NW (da Rosa et al., 2016, and references therein). The evidence collected, while consistent, is not ubiquitous throughout the state and confined to the sites where structures have been identified.

Here, we present paleocurrent direction results obtained from an extensive anisotropy of magnetic susceptibility (AMS) study conducted on a variety of lithologies of the Itararé Group sedimentary rocks collected throughout the state of São Paulo that do not possess visible ice-flow indicators. Such detailed study, coupled with extensive rock-magnetic evidence, compliments the more regional study of Raposo et al. (2020), which includes a partial set of the AMS data from São Paulo state presented here. The paleocurrent directions obtained from AMS are consistent with the direct observations of ice-flow kinematics and sediment transport. Additionally, we investigate the depositional environments of the Itararé Group rocks by means of the  $q$ – $\beta$  empirical method of Taira (1989) that is based on AMS fabrics. Such analysis further proves that the magnetic fabrics are primary and were acquired under a range of sedimentary depositional regimes that are consistent with the sedimentary and stratigraphic interpretations.

## 2. Materials and Methods

The Itararé Group sedimentary rocks were sampled at 33 different localities that span the eastern portion of the state of São Paulo from north to south and into the southernmost portion of the state of Minas Gerais. The collected sites comprise gray to tan-colored diamictites, fine yellow sands and siltstones, coarse sand, thinly laminated gray rhythmites, competent claystones, red mudstones, and red sandy mudstones. Geographic coordinates for the sampling sites are reported in table 1 and Figure 1, whereas selected field photographs of the sampled lithologies are shown in Figure 2. The collected sites consist of flat-laying deposits,

**Table 1**  
*Site Location and Site-Mean AMS Parameters for the Itararé Group Rocks*

Site	Lithology	Lat (°)	Long (°)	<i>n</i>	Site-mean AMS results														
					Min ( $K_3$ )	$D_{\min}$	$I_{\min}$	Int ( $K_2$ )	$D_{\text{int}}$	$I_{\text{int}}$	Max ( $K_1$ )	$D_{\max}$	$I_{\max}$	$L$	$F$	$P_J$	$T$	$q$	$\beta$ (°)
IT1*	Sandstone	−23.3339	−47.3238	14	0.330	177	84	0.335	17	5	0.335	287	2	1.001	1.015	1.014	0.875	0.24	12
IT2*	Rhytmite	−23.2656	−47.3244	42	0.288	177	88	0.353	25	2	0.359	295	1	1.017	1.226	1.208	0.848	0.11	8
IT3	Diamictite	−23.2299	−47.4354	41	0.305	301	80	0.337	75	7	0.357	166	7	1.060	1.104	1.142	0.256	0.51	16
IT4	Turbidite	−23.2234	−47.5728	20	0.332	289	71	0.334	131	18	0.334	39	7	1.001	1.005	1.005	0.672	0.48	28
IT5geo	Shale	−23.2232	−47.5737	65	0.328	226	81	0.333	55	9	0.340	325	2	1.022	1.015	1.033	−0.175	0.79	21
IT5strat	Shale	−23.2232	−47.5737	65	0.330	76	61	0.331	239	28	0.340	333	7	1.027	1.003	1.030	−0.768	0.79	47
IT6	Pelodite	−23.1368	−47.6836	54	0.331	165	79	0.334	295	7	0.336	26	8	1.005	1.010	1.012	0.310	0.54	29
IT7	Sandstone	−23.1156	−47.7268	28	0.331	128	86	0.334	3	3	0.334	273	4	1.001	1.008	1.008	0.839	0.11	7
IT8*	Sandstone	−23.1180	−47.7164	28	0.332	235	69	0.334	106	14	0.334	12	16	1.002	1.007	1.007	0.608	0.51	28
IT10	Siltstone	−23.1163	−47.7327	56	0.331	257	87	0.334	97	3	0.335	7	1	1.003	1.009	1.010	0.543	0.42	13
IT11	Sandstone	−23.1160	−47.7363	26	0.331	256	76	0.334	348	0	0.335	78	14	1.002	1.009	1.009	0.644	0.33	23
IT12	Sandstone	−23.1109	−47.7459	38	0.332	242	82	0.334	124	4	0.334	33	7	1.000	1.005	1.005	0.824	0.24	12
IT13	Siltstone	−23.1109	−47.7459	39	0.331	325	77	0.334	78	5	0.335	169	12	1.002	1.010	1.011	0.605	0.37	18
IT16	Diamictite	−23.0851	−47.7836	59	0.331	1	84	0.334	186	6	0.335	96	0	1.001	1.010	1.010	0.796	0.41	22
II1*	Claystone	−23.5427	−47.6494	39	0.329	20	88	0.335	217	2	0.336	127	1	1.001	1.018	1.017	0.873	0.25	9
II2*	Claystone	−23.5439	−47.6542	30	0.322	357	88	0.339	173	2	0.339	263	0	1.001	1.050	1.045	0.950	0.05	4
II3	Claystone	−23.5440	−47.6571	35	0.323	96	87	0.338	4	0	0.339	274	3	1.002	1.048	1.044	0.909	0.10	7
II4	Diamictite	−23.5456	−47.6808	37	0.332	318	79	0.334	194	6	0.334	103	9	1.002	1.006	1.007	0.536	0.47	23
II5	Siltstone	−23.5438	−47.6922	55	0.333	312	37	0.333	104	49	0.334	211	14	1.003	1.002	1.004	−0.133	0.64	53
II6	Diamictite	−23.5381	−47.7125	39	0.315	158	69	0.339	47	8	0.347	314	20	1.023	1.076	1.085	0.528	0.31	25
II7	Diamictite	−23.5812	−47.9358	28	0.320	310	71	0.335	202	6	0.345	110	18	1.030	1.046	1.066	0.208	0.50	20
II8	Sandstone	−23.6895	−48.1086	21	0.330	293	81	0.334	109	9	0.336	199	1	1.006	1.012	1.015	0.379	0.64	27
II9	Siltstone	−23.7889	−48.1360	49	0.327	187	75	0.335	74	6	0.337	342	14	1.006	1.025	1.027	0.613	0.29	18
II10	Diamictite	−23.9242	−48.2849	39	0.321	289	82	0.339	34	2	0.340	124	8	1.002	1.056	1.051	0.919	0.22	14
II11	Sandstone	−23.8797	−49.3847	28	0.329	270	85	0.335	164	1	0.336	74	5	1.003	1.020	1.019	0.776	0.27	12
II12	Sandstone	−20.9927	−46.9749	43	0.332	142	80	0.334	317	10	0.334	47	1	1.001	1.007	1.007	0.699	0.32	15
II13	Red beds	−20.8932	−46.9459	46	0.324	250	85	0.337	140	2	0.340	50	5	1.009	1.040	1.041	0.620	0.27	9
II14	Diamictite	−22.7577	−47.4698	48	0.333	344	43	0.333	250	5	0.334	155	46	1.002	1.001	1.003	−0.033	0.64	59
II15	Diamictite	−22.7478	−47.5028	45	0.320	280	84	0.340	56	4	0.341	146	4	1.003	1.062	1.057	0.906	0.27	15
II16*	Siltstone	−22.7476	−47.5066	18	0.331	186	84	0.334	340	5	0.335	70	2	1.002	1.008	1.008	0.613	0.32	18
II17	Rhytmite	−22.9209	−47.1335	21	0.324	167	88	0.338	298	2	0.338	28	2	1.001	1.043	1.039	0.957	0.08	5
II18	Red beds	−21.7370	−47.0712	11	0.328	128	73	0.336	324	16	0.337	232	4	1.002	1.025	1.024	0.866	0.33	18
II19	Red beds	−21.1201	−46.8708	33	0.327	221	84	0.335	348	4	0.338	78	5	1.007	1.026	1.028	0.558	0.33	17
II20*	Rhytmite	−23.2498	−47.3294	22	0.320	276	87	0.339	60	2	0.341	150	2	1.004	1.061	1.056	0.888	0.08	5

*Note.* *n*, number of specimens used to calculate the mean fabrics;  $K_1$ ,  $K_2$ , and  $K_3$  are the eigenvalues of the maximum, intermediate, and minimum anisotropy principal axes, respectively, with eigenvector orientations labeled  $D_{\max}$ ,  $I_{\max}$ , etc. (the asterisked site means were eliminated from the imbrication analysis to determine paleocurrent direction, see text for details);  $L$ ,  $F$ ,  $P_J$ , and  $T$  are the magnetic lineation (Balsley & Buddington, 1960), foliation (Stacey et al., 1960), corrected degree of anisotropy, and shape parameter (Jelinek, 1981),  $q$  is the  $L/F$  parameter of Granar (1957), whereas  $\beta$  (°) is the imbrication angle in degrees relative to the bedding plane (see text for details on all these parameters).

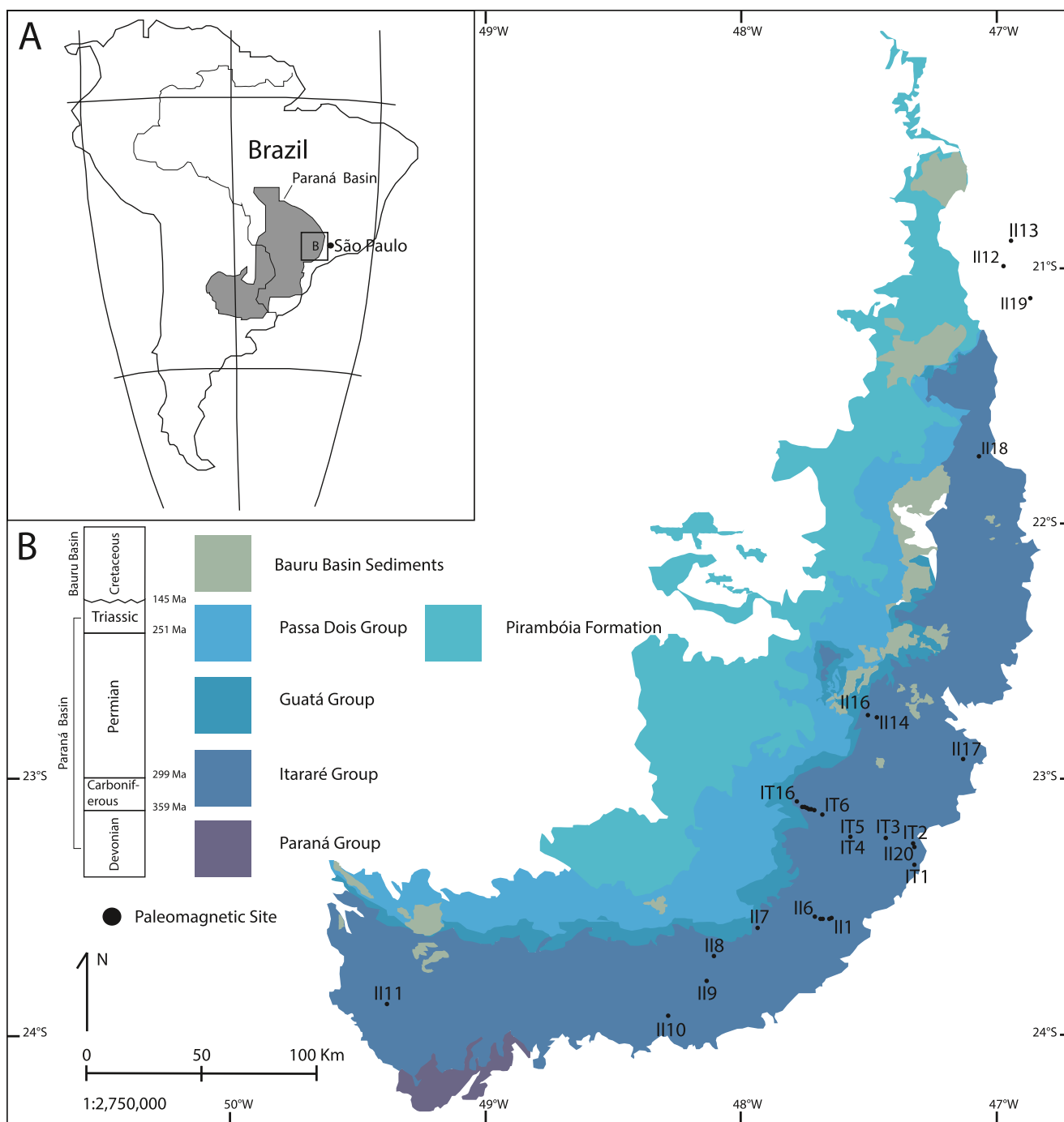


**Figure 1.** Simplified geologic map of the study area: inset shows the extent of the Paraná Basin. Main map shows the extent of the Itararé Group rocks within the state of São Paulo, on the eastern margin of the Basin, and the sampling site locations, three sites to the north are located in the adjacent state of Minas Gerais. Where sampling sites are distributed along transects, only the site names at each end are reported on the map, see Table 1 for site locations.

with the exception of one site (IT5) which is affected by slumping. Three igneous sills were collected at sites IT9, IT14, and IT15 and will not be reported here (see Bilardello et al., 2018, for details about these sites).

Rock cores were drilled using a water-cooled gasoline drill and oriented with a Pomeroy orienting fixture with a magnetic compass and whenever possible using a sun-compass. Cores were cut into  $2.5 \times 2.2$  cm sized paleomagnetic cylinders. The number of specimens collected from each site varied depending on their competency and general interest on the specific outcrop. The number of specimens ranges from a minimum





**Figure 2.** Selected field photographs of the lithologies sampled—(a) site IT1: intercalated fine to medium sandstones and silts at the Basin's eastern margin and interpreted as delta deposits; (b) site IT2: gray rhythmite with intercalated muds and fine sands with fine scale sedimentary structures (trough and climbing ripples) and drop stones (coin for scale); (c) site IT5: gray shale affected by sedimentary slumping, backpack for scale; (d) site IT6: gray pelodite, structureless mixture of silt and clay, drill holes for scale (2.5 cm diameter); (e) site IT8: medium yellow sandstone, the section is massive at the base (not shown in the picture) and becomes more stratified toward the top, with cross-bed trough stratification, drill holes for scale; (f) site IT12: yellow channel sandstone overlain by reddish conglomerate, cutting into greenish layered siltstone and mudstone (site IT13) the entire outcrop is ~5-m thick; (g) site II1: gray-tan claystone with silt, very hard and competent with conchoidal fractures and featuring sand intercalations with iron nodules, drill holes marked by arrow for scale; (h) site II6: gray diamictite with cm-size granite clasts (marked by arrow); (i) site II18: red sandy claystone matrix with iron concretions and intercalated yellowish sandy layers, outcrop ~5 m in height.

of 11 standard cylinders for an incompetent sandy red bed outcrop, to a maximum of 65 for the slumped shale outcrop sampled at site IT5, for which more detail was sought. Overall, an average of 36 specimens was investigated per site.

Rock-magnetic measurements on specimens from all sites were conducted at the Institute for Rock Magnetism, University of Minnesota. Hysteresis loops were measured on Princeton Measurements Corporation (Princeton, NJ, USA) 3900 MicroMag Vibrating Sample Magnetometers in fields up to 1 or 1.5 T. DC and AC magnetic experiments were conducted on Quantum Design (San Diego, CA, USA) Magnetic Properties Measurement Systems (MPMSs). DC experiments included measuring magnetic remanence upon heating from 20 K to room temperature after cooling in a 2.5 T field (field cooled remanence, FC), and after cooling in zero field but applying a saturation isothermal remanent magnetization (SIRM) of 2.5 T at 20 K (zero-field cooled remanence, ZFC). A room temperature (RT) 2.5 T SIRM was also applied and the remanence measured upon cooling to 20 K and warming back to room temperature (RTSIRM). The “goethite test” (e.g., Guyodo et al., 2006) was applied to selected specimens, whereby specimens were cooled from 400 to 300 K in the presence of a 2.5 T field. The partial thermal remanent magnetization was then measured (in zero field) upon cooling and warming between 300–20–300 K (pTRM cooling and warming curves). The specimens were then taken out of the MPMS and AF demagnetized using 200 mT AC fields to eliminate the contribution of soft phases like magnetite and reinserted in the MPMS. The magnetic remanence was then thermally cycled between 300–20–400 K (post-AF cooling and warming curves) to thermally demagnetize the contribution of goethite, and then again between 400–20–300 K (post-400 K cooling and warming curves). The last measurement cycle likely reflects the contribution of hematite only, and/or hard magnetic phases with Curie temperatures higher than 400 K (e.g., nanomaghemite [Carter-Stiglitz et al., 2001;

Smirnov & Tarduno, 2000)], if present. Mass-normalized AC in-phase and out-of-phase susceptibilities ( $\chi'$  and  $\chi''$ , respectively, units of  $\text{m}^3/\text{kg}$ ) were measured as a function of frequency and temperature between 10 and 300 K using seven frequencies logarithmically spaced between 1 and 1,000 Hz.

AMS measurements for specimens from sites IT1 through IT16 were performed at the Instituto de Geociencias, University of São Paulo, Brazil (IGc-USP) on an AGICO (Brno, Czech Republic) KLY-4S susceptibility bridge equipped with a single-axis rotator, in AC fields of 300 A/m at 875 Hz frequency. Specimens from sites II1-20 were measured at the Institute for Rock Magnetism using an AGICO MFK1-FA equipped with a single-axis rotator, in AC fields of 200 A/m at 976 Hz frequency. Anisotropy data were processed using the Pmag.Py software package (Tauxe et al., 2016) and principal axes reported are normalized so that their sum equals unity. Magnetic lineation ( $L$ ) and foliation ( $F$ ) are calculated as  $K_1/K_2$  and  $K_2/K_3$ , following Balsley and Buddington (1960) and Stacey et al. (1960), respectively, whereas the shape parameter  $T = (2\eta_2 - \eta_1 - \eta_3) / (\eta_1 - \eta_3)$ , and the corrected degree of anisotropy  $P_J = \exp \sqrt{2 \left[ (\eta_1 - \eta_m)^2 + (\eta_2 - \eta_m)^2 + (\eta_3 - \eta_m)^2 \right]}$ , where  $\eta_1 = \ln K_1$ ,  $\eta_2 = \ln K_2$ ,  $\eta_3 = \ln K_3$ ,  $\eta_m = \sqrt[3]{\eta_1 \cdot \eta_2 \cdot \eta_3}$ , are calculated following (Jelinek, 1981).

### 3. Results

#### 3.1. Low-Temperature Magnetometry

Low-temperature DC magnetic experiments conducted on representative specimens from all lithologies indicate that for most specimens the FC and ZFC curves are separated at low temperature and upon warming join at  $\sim 250$  K or higher (Figures 3a and 3, left side panels). A few specimens exhibit little to no separation of the FC and ZFC curves, and these either decrease rapidly upon warming between low temperature and  $\sim 40$  K, or more gradually to room temperature (Figures 3e and 3h, left side panels, respectively). The majority of specimens possess FC-ZFC curves with an inflection around 120 K (Figures 3e–3h, left side panels). RTSIRM curves on cooling and warming always possess an inflection at  $\sim 120$  K (Figures 3a and 3, left side panels) and sometimes a higher temperature inflection  $\sim 250$ – $260$  K (Figures 3f–3h, left side panels). The goethite tests reveal variable separation between the pTRM cooling and warming curves between 300 and  $\sim 120$  K (Figures 3b–3d, left side panels). For all specimens, a considerable amount of remanence is removed by the AF demagnetization, while some remanence is removed by the 400 K thermal demagnetization (Figures 3b–3d, left side panels). After thermal demagnetization, an inflection around 230–250 K, sometimes accompanied by thermal hysteresis in the cooling–warming curves, is sometimes apparent in the final temperature cycling (Figures 3b and 3d, left side panels).

In-phase AC susceptibility  $\chi'$  of all specimens is dominated by paramagnetic Curie–Weiss  $\sim 1/T$  behavior. For many specimens, peaks occur between  $\sim 200$  and 240 K that also display frequency dependence (Figures 3b, 3c, 3f, and 3g, right side panels). Some specimens have peaks around 120 K (Figures 3g and 3f, right side panels), whereas one specimen has a prominent peak centered at 20 K (Figure 3g, right hand panel). Out-of-phase susceptibility  $\chi''$  has frequency-dependent peaks at similar 200–230 K temperatures as  $\chi'$  (Figures 3b, 3c, 3f, and 3g, right side panels), with one of the specimens displaying a  $\sim 240$  K  $\chi''$  peak that is absent in  $\chi'$  (Figure 3a, right side panel). Other specimens do not possess distinct peaks in  $\chi''$ , but instead have a broad curvature that displays frequency dependence, albeit with some measurement noise, particularly at the highest frequencies (Figures 3d and 3h, right hand panel).

#### 3.2. Room Temperature Magnetic Hysteresis

Hysteresis loops measured at room temperature on representative specimens from each lithology are plotted in Figure 4. Before paramagnetic slope correction the loops are narrow and pass through the origin, indicating little hysteresis and curvature. After correcting for the paramagnetic slope these loops indicate the weakest magnetizations overall. A small number of loops display increased curvature, but are also narrow, and reveal weak magnetizations after paramagnetic slope correction, for example the gray diamictite at site II6. Other loops, instead, are more open and often constricted at the origin (e.g., the brown diamictite at site II10, the red beds at site II13, the brown-tan rhythmite at site II20, and the white-pink sandstone

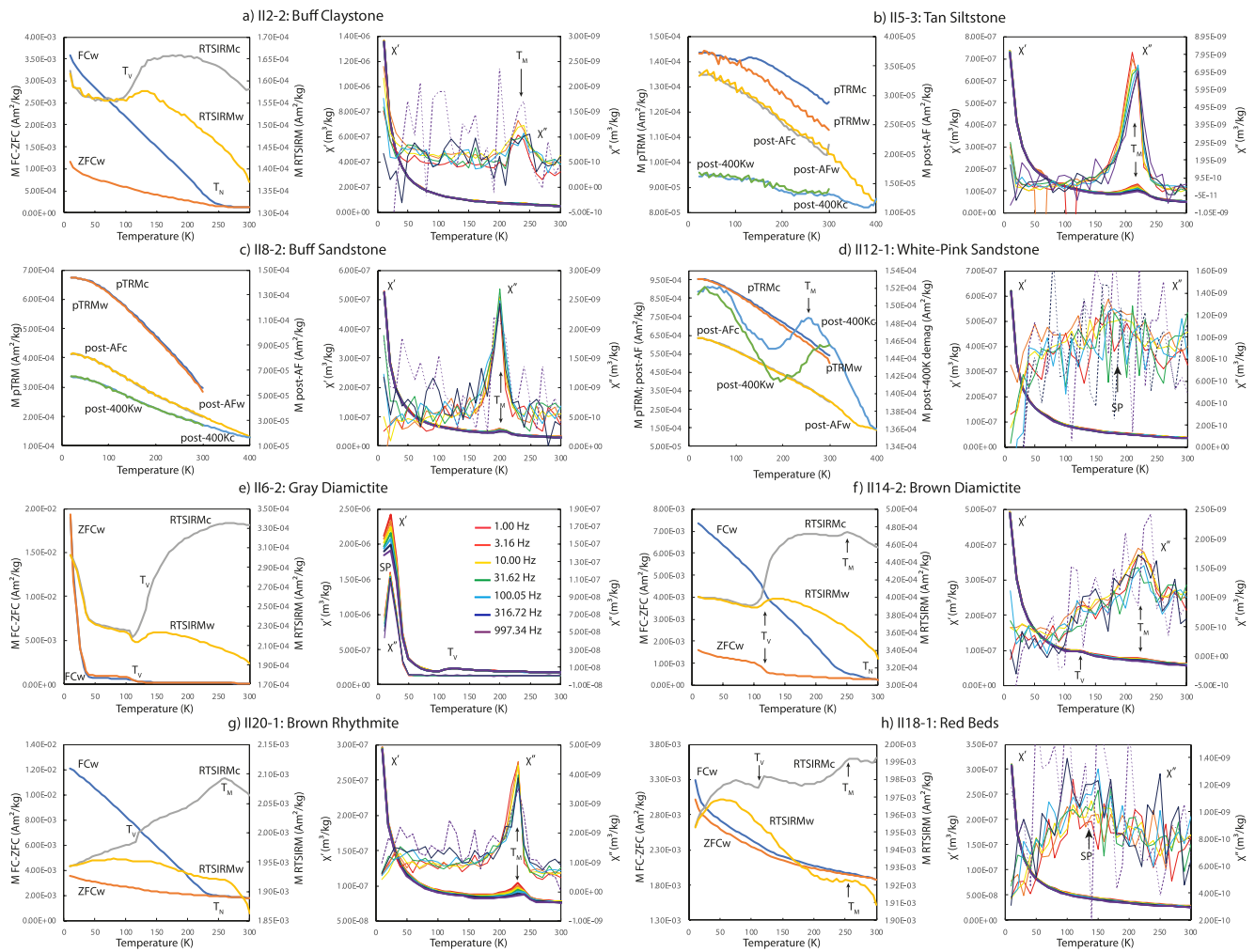


**Figure 3.** Low-temperature magnetometry for representative specimens separated by lithology. For each rock type the left side panels are DC magnetic remanences, whereas the right side panels are in-phase ( $\chi'$ ) and out-of-phase ( $\chi''$ ) AC susceptibilities. (a, e–h) FC-ZFC-RTSIRM cooling and warming curves; (b–d) “goethite test” results (e.g., Guyodo et al., 2006), all curves are labeled by type.  $T_M$  and  $T_V$  indicate the hematite Morin and the magnetite Verwey transitions, respectively.  $T_N$  indicates goethite’s blocking temperature (below the Néel temperature), while SP indicates broad superparamagnetic grain blocking temperature that do not coincide with either  $T_M$  or  $T_V$  (see text for details). Some dotted  $\chi''$  curves for the highest frequency measured indicate higher measurement noise that distracts from the general pattern.

at site II12). Despite these loops indicating a distribution of ferrimagnetic coercivity, the intensities of the magnetizations at saturation remain low.

### 3.3. Anisotropy of Magnetic Susceptibility

The majority of sites possess bedding parallel magnetic fabrics, with subvertical minimum principal axes,  $K_3$ , and subhorizontal intermediate and maximum principal axes,  $K_2$  and  $K_1$  (Figure 5a). Exceptions to the general trend are sites II5 and II14 that possess a strongly imbricated fabric with  $K_3$  axes plunging to the NW and NNW, respectively, and will be described in more detail below (Figures 5a, 5c, and 5d; Table 1). Sites II5 and II14 have been excluded from calculating a mean fabric. Likewise, site IT5 has also been excluded from the Group mean because it is affected by folding, as discussed below. At the Group level,  $K_3$  axes are somewhat girdled, with an elongation oriented NW-SE, whereas the  $K_1$  axes are somewhat dispersed within the horizontal plane with a preferred orientation of NW-SE (Figure 5b). On either a Flinn diagram (Flinn, 1978) or Jelinek plot (Jelinek, 1981), the shape of the fabrics for the individual site-mean fabrics/lithologies is predominantly triaxial-oblate to oblate, with anisotropy varying between a few percent to under 25% (Figures 5c and 5d).



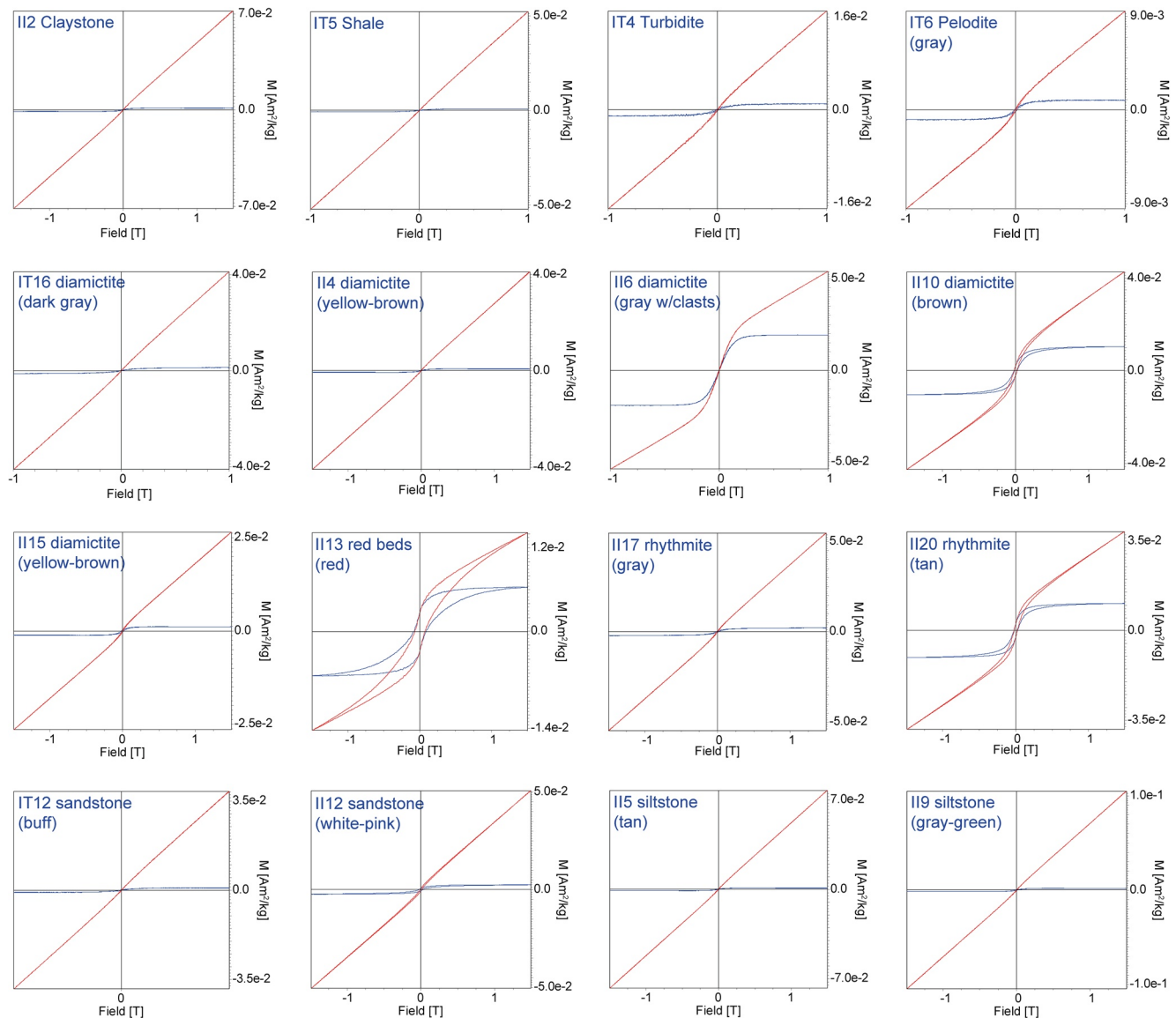


**Figure 4.** Hysteresis loops for representative specimens from each lithology. Red/blue are loops uncorrected/corrected for paramagnetic slope, respectively. All loops indicate weak magnetizations at saturation after paramagnetic slope correction, with the majority of the loops remaining narrow throughout and displaying little hysteresis (see text for details).

A few sites possess triaxial fabrics, and, with the exception of sites II5 and II14 mentioned above, their site-mean fabrics possess subvertical  $K_3$  axes and subhorizontal  $K_1$  axes. Some examples of these are the slumped shale at site IT5, the tan and gray diamictites at sites IT3 and IT7, and the pelodite at site IT6. In geographic coordinates, site IT5 possesses distinct principal axes orientation, with the  $K_2$  and  $K_3$  axes somewhat elongated toward each other, as reflected by their confidence ellipses and the triaxial shape of the site-mean fabric, when evaluating the cumulative distribution of the bootstrapped eigenvalues (Figure 6a). In stratigraphic coordinates, however, the  $K_2$  and  $K_3$  axes are truly girdled, and the shape of the site-mean fabric tends to prolate, though the cumulative distributions of the  $K_2$  and  $K_3$  eigenvalues remain distinct at the 95% confidence interval (Figure 6b). Site II5 represents 55 specimens collected from a flat-laying siltstone that is void of sedimentary structures. The fabric for II5 is triaxial-prolate, with distinct principal axes, and subhorizontal  $K_1$  axes and elongated  $K_2$  and  $K_3$  axes within the plane that contains them. The  $K_3$  axes plunge  $\sim 40^\circ$  to the NW (Figure 6c). The yellow-brown diamictite collected at site II14 has an AMS fabric characterized by  $K_3$  axes plunging  $\sim 40^\circ$  to the NNW and  $K_1$  axes plunging  $\sim 50^\circ$  to the SSE. The  $K_2$  and  $K_3$



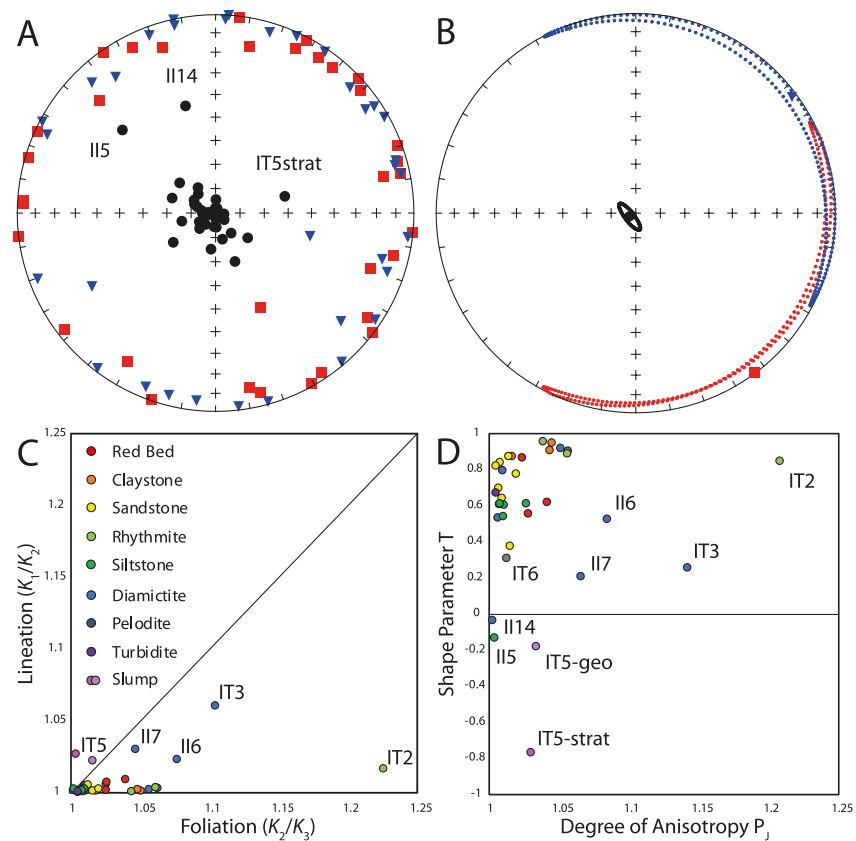


**Figure 5.** Site-mean AMS fabric. (a) Data plotted on a lower hemisphere stereonet (red squares, blue triangles, and black dots are the site-mean maximum  $K_1$ , site-mean intermediate  $K_2$ , and site-mean minimum  $K_3$ , principal axes, respectively); (b) mean anisotropy principal axes and 95% confidence ellipses plotted on a lower hemisphere stereonet, excluding sites IT5, II5, and II14 (symbol colors as in panel a); (c) Flinn diagram of site-mean AMS data color coded by lithology, as per legend in the panel, with some relevant triaxial or highly anisotropic site-mean data labeled; (d) Jelinek plot (Jelinek, 1981), showing the shape parameter  $T$  versus the corrected degree of anisotropy  $P_j$  for all data as in panel (c) (see text for details).

principal axes are somewhat elongated toward each other, but their eigenvalues are distinct, defining a triaxial fabric that tends to prolate (Figure 6d). Examples of sites with triaxial, triaxial-oblate fabrics are from sites IT3 and II7. These have bedding parallel to slightly imbricated fabric orientations, with well-grouped principal axes and  $K_1$  and  $K_2$  axes distributed within the plane that contains them (Figure 6e), similarly to the predominant sites with oblate, triaxial-oblate fabrics (Figure 5). The pelodite at site IT6, a lithified resedimented glacial flour, is flat-laying, undeformed, and void of sedimentary structures, yet its magnetic fabric is triaxial-prolate and the  $K_2$  and  $K_3$  principal axes are somewhat elongated within the same plane, with subvertical  $K_3$  axes and subhorizontal  $K_1$  axes (Figure 6f). This site will be discussed further below.

#### 4. Discussion

Magnetic remanence as a function of temperature experiments indicate mixtures of magnetic minerals for the Itararé Group rocks. In the DC experiments, the separation of the FC-ZFC curves at low temperature, which join upon heating at  $\sim 250$  K or higher (Figures 3a and 3), is indicative of nanogoethite that possesses unblocking temperatures somewhat below the Néel temperature ( $T_N$ ) of fully crystalline goethite ( $\sim 393$  K). The decreases in remanence  $\sim 120$  and  $250$  K in the FC-ZFC and/or RTISIRM cooling and warming curves correspond to the magnetite Verwey ( $T_V$ ) and hematite Morin ( $T_M$ ) transitions, respectively. The nonrecovery of magnetization from the temperature cycling of the RTISIRM suggests that multidomain magnetite is responsible for the magnetization lost (Figures 3a and 3). Likewise, the curvature, or humpiness, of these curves is indicative of oxidized magnetite (Özdemir & Dunlop, 2010).

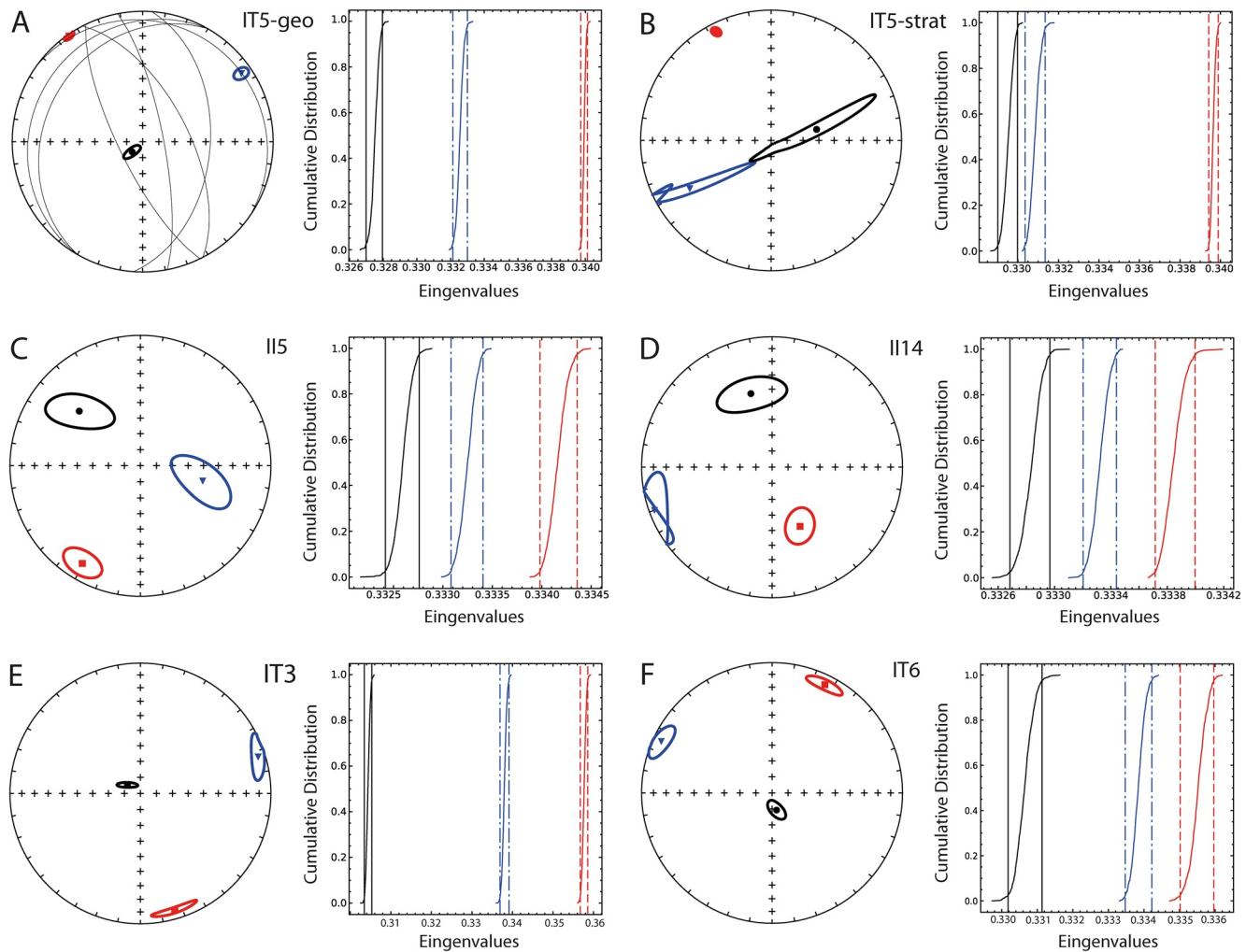


**Figure 6.** Site-mean AMS data and 95% confidence ellipses for sites that possess triaxial fabrics plotted on lower hemisphere stereonets and as cumulative distributions of the eigenvalues: (a) slumped shale at site IT5 in geographic coordinates, black solid lines are the sampled bedding planes, and in stratigraphic coordinates in (b). Upon untilting the fabric evolves from triaxial-prolate to prolate, with progressive girdling of the  $K_2$  and  $K_3$  principal axes (red, blue, and black are  $K_1$ ,  $K_2$ , and  $K_3$ , respectively); (c, d) The triaxial-prolate fabrics for the siltstone at site II5 and the yellow-drown diamictite at site II14, with strongly imbricated fabrics (cf., Figure 4a). These possess  $K_2$  and  $K_3$  principal axes distributed within the same plane; (e) triaxial-oblate fabric for gray diamictite at site IT3, which has similar orientation to the majority of the Itararé Group rocks with oblate, triaxial-oblate fabrics; (f) triaxial-oblate fabric of the pelodite at site IT6 with some elongation of the  $K_3$  principal axis distribution (see text for details).

The remanence removed during the AF demagnetization in the goethite test-experiments reflects removal of soft magnetic contributions, likely from magnetite or nanohematite (e.g., Roberts et al., 2020) (Figures 3b–3d). The remanence removed through heating of the specimens to 400 K in the same experiments is attributed to goethite but could in part be attributed to nanomaghemite, as suggested by the increase in remanence toward low temperature of the final temperature cycling after the 400 K demagnetization (Carter-Stiglitz et al., 2001; Smirnov & Tarduno, 2000). Finally, the inflection of these curves  $\sim 250$  K (Figure 3b) and the prominent thermal hysteresis observed in Figure 3d are attributed to hematite cycling across the Morin transition.

Magnetic susceptibility experiments as a function of frequency and temperature indicate that the in-phase susceptibility  $\chi'$  largely reflects the paramagnetic contribution to the samples, with superimposed hematite and magnetite contributions below room temperature (Figures 3b, 3c, and 3). For the gray diamictite specimen at site II6, a narrow superparamagnetic (SP) blocking temperature peak is present at 20 K (Figure 3e). The out-of-phase susceptibility  $\chi''$  instead appears to be particularly sensitive to the hematite Morin transition at temperatures ranging between  $\sim 200$  and 250 K, with the position of the peak reflecting different

grain sizes (Figures 3a–3c, 3f, and 3). In fewer cases,  $\chi''$  reveals the magnetite Verwey transition (Figures 3e and 3f). As for the  $\chi'$  peak, the 20 K  $\chi''$  peak for the specimen at site II6 is interpreted as a SP blocking temperature (Figure 3e). In two other specimens, a white-pink sandstone and a red bed,  $\chi''$  does not reveal a distinctive peak associated with either the  $T_M$  or the  $T_V$  observed in the DC experiments but instead possesses a broader arch with maximum susceptibilities around 175 and 125 K (Figures 3d and 3h). For both these lithologies, the DC experiments indicate a hematite  $T_M$  at  $\sim 250$  K. Additionally, temperature cycling of the RTSIRM curves for the sandstone reveals some nonrecovery of remanence when warming above 100 K, while for the red bed specimen a magnetite  $T_V$  at 120 K is also present. The arch is thus interpreted as a broad blocking temperature spectrum for grains in a SP state, likely magnetite.

Hysteresis data show that the majority of the Itararé Group rocks at room temperature are dominantly paramagnetic, with narrow hysteresis loops that for most sites resemble straight lines that pass through the origin with steep positive slope (Figure 4). After subtraction of the paramagnetic slope, the loops indicate low saturation magnetization ( $M_S$ ) and remanent magnetization ( $M_R$ ), consistently with low concentrations of ferromagnetic grains (*s.l.*). The hysteresis loops for a minority of sites have more curvature, indicating increased ferromagnetic (*s.l.*) content (e.g., the gray diamictite at II6), yet, the loops are narrow and have low  $M_S$  and even lower  $M_R$  after paramagnetic correction, indicating a mixture of SP and multidomain magnetite grains. A few loops are wider and constricted at the origin (e.g., the red bed at II13, the II20 rhythmite, and the II10 diamictite), reflecting coercivity contrasts (e.g., Tauxe et al., 1996), consistently with the low-temperature evidence for presence of magnetite and hematite.

#### 4.1. Origin of the AMS

Provided the dominant paramagnetic behavior of the Itararé Group rocks at room temperature, most AMS fabrics are interpreted to reflect the attitude of the paramagnetic phases in the samples. For the lithologies with increased ferromagnetic (*s.l.*) mineral content, the AMS is instead likely carried by these grains, whether magnetite, hematite, or SP grains.

The orientation of the AMS fabrics, bedding parallel to somewhat imbricated (Figures 5 and 6), allows interpreting the majority of the fabrics as primary sedimentary compactional fabrics and sedimentary fabrics deposited in a current, respectively (e.g., Bilardello, 2016; Jackson & Tauxe, 1991; Kodama, 2012; Tarling & Hrouda, 1993). In a paleomagnetic study conducted on the same Itararé Group rock specimens, Bilardello et al. (2018) had determined that these rocks had been affected by Cretaceous remagnetizations. The responsible heating or hydrothermal events, however, do not appear to have affected the attitude of the AMS fabrics recorded. Magmatic events responsible for remagnetizations have generally found not to affect AMS fabrics in natural and synthetic rocks, and in certain cases were even found to enhance remanent fabrics by secondary growth of magnetic minerals along the preexisting fabric (e.g., Borradaile & Lagroix, 2000; Henry et al., 2003; Li & Kodama, 2005). Where heating was found to negatively affect the AMS, it resulted in a weakening of the fabric and increased dispersion of the principal anisotropy axes (Li & Kodama, 2005), which is not observed in the Itararé Group rocks.

Exceptions for the interpretation of primary sedimentary fabrics are the slumped shale at site IT5, and the two strongly imbricated triaxial fabrics observed for the siltstone at site II5 and the diamictite at site II14. The attitudes of the magnetic fabrics before and after tilt correction for site IT5 (cf., Figures 6a and 6b) indicate better clustering of the AMS principal axes in geographic coordinates, similarly to the better grouping of paleomagnetic directions for the same site reported in Bilardello et al. (2018). The AMS fabric in geographic coordinates is thus interpreted to have been acquired after the slumping event and represents gravitational/compactional reorientation of the grains in a wet sediment. The fabric, therefore, represents a superposition of a compactional and deformation fabric, where the magnetic lineation, subparallel to the fold axes, constitutes an intersection lineation acquired during slumping (e.g., Bilardello, 2016; Bilardello & Kodama, 2009; Housen et al., 1993; Weil & Yonkee, 2009). Following this interpretation, the fabric of site IT5 is not used for any paleocurrent analysis. The AMS fabrics for sites II5 and II14 (Figures 6c and 6d) are more difficult to interpret: the  $\sim 50^\circ$  offset of the  $K_3$  axes from the pole to bedding is too large to be attributed to any sedimentary process as grains become unstable at these angles (Novak et al., 2014) and no deformation structures were observed. We exclude the fabrics from these sites from the paleocurrent analysis.

Representative site-mean fabrics on the map of the Itararé Group, plotted with their confidence ellipses around the mean principal axes, are reported in Figure 7. As discussed above, the fabrics for the different lithologies vary widely from oblate to triaxial and in degree of anisotropy, invalidating the calculation of average fabrics for sites that are proximal to each other. In general, the more oblate fabrics tend to be subparallel to the bedding plane, with steep  $K_3$  axes and  $K_1$  and  $K_2$  axes dispersed in the horizontal plane, determining poorly defined magnetic lineations (e.g., sites II17 and II16). These fabrics represent sedimentary/compactional fabrics resulting from deposition under low current conditions (e.g., Bilardello, 2016; Kodama, 2012; Martín-Hernández et al., 2004; Taira, 1989; Tarling & Hrouda, 1993). However, oblate fabrics also possess increasing imbrication with respect to bedding, yet not necessarily parallel to the magnetic lineation (e.g., sites II9, II10, II11, II12, and IT13). The degree of imbrication tends to increase for increasingly triaxial fabrics, however, as for the more oblate fabrics, the imbrication can parallel the  $K_2$  principal axes (e.g., sites II8, II12, and II16), or neither the  $K_1$  or  $K_2$  axes, defining magnetic foliations that are somewhat oblique with respect to bedding (e.g., II4, II7, II18, and IT4). The orientation of the magnetic lineation within a grain is controlled by grain shape in minerals with shape anisotropy, like magnetite, or is parallel to the crystallographic  $a$ -axes for the paramagnetic susceptibility of most phyllosilicate grains (e.g., Biedermann, 2018; Borradaile & Werner, 1994). For minerals that possess magnetocrystalline anisotropy, like hematite, the lineation may lie anywhere within the platelets' basal plane (e.g., Biedermann, 2018; Guerrero-Suarez & Martín-Hernández, 2012; Hrouda, 2002; Martín-Hernández and Guerrero-Suárez, 2012), or parallel the distribution of iron-bearing inclusions in phyllosilicate minerals (e.g., Biedermann, 2018; Borradaile & Werner, 1994; Lagroix & Borradaile, 2000; Martín-Hernández & Hirt, 2003; Parés & van der Pluijm, 2002). The orientation of the low-field magnetic susceptibility lineation is therefore not always a reliable indicator of particle alignment in a current and may in fact reflect the alignment of iron inclusions in phyllosilicate grains, and/or the intersection lineation of ferromagnetic (s.l.) or paramagnetic minerals. However, for site-mean fabrics where the distribution of the  $K_3$  principal axes is elongated, the orientation of their elongation is often parallel to the direction of imbrication, reflecting variable angles of repose of the mineral platelets and reflecting paleocurrent orientation. The mean plunge of the minimum axis of the site-mean fabric is thus the most reliable indicator of paleocurrent direction, particularly when elongated, and not the lineation, as is generally reported for ferrimagnetic grains with shape anisotropy (e.g., Jackson & Tauxe, 1991; Kodama, 2012; Martín-Hernández et al., 2004; Tarling & Hrouda, 1993).

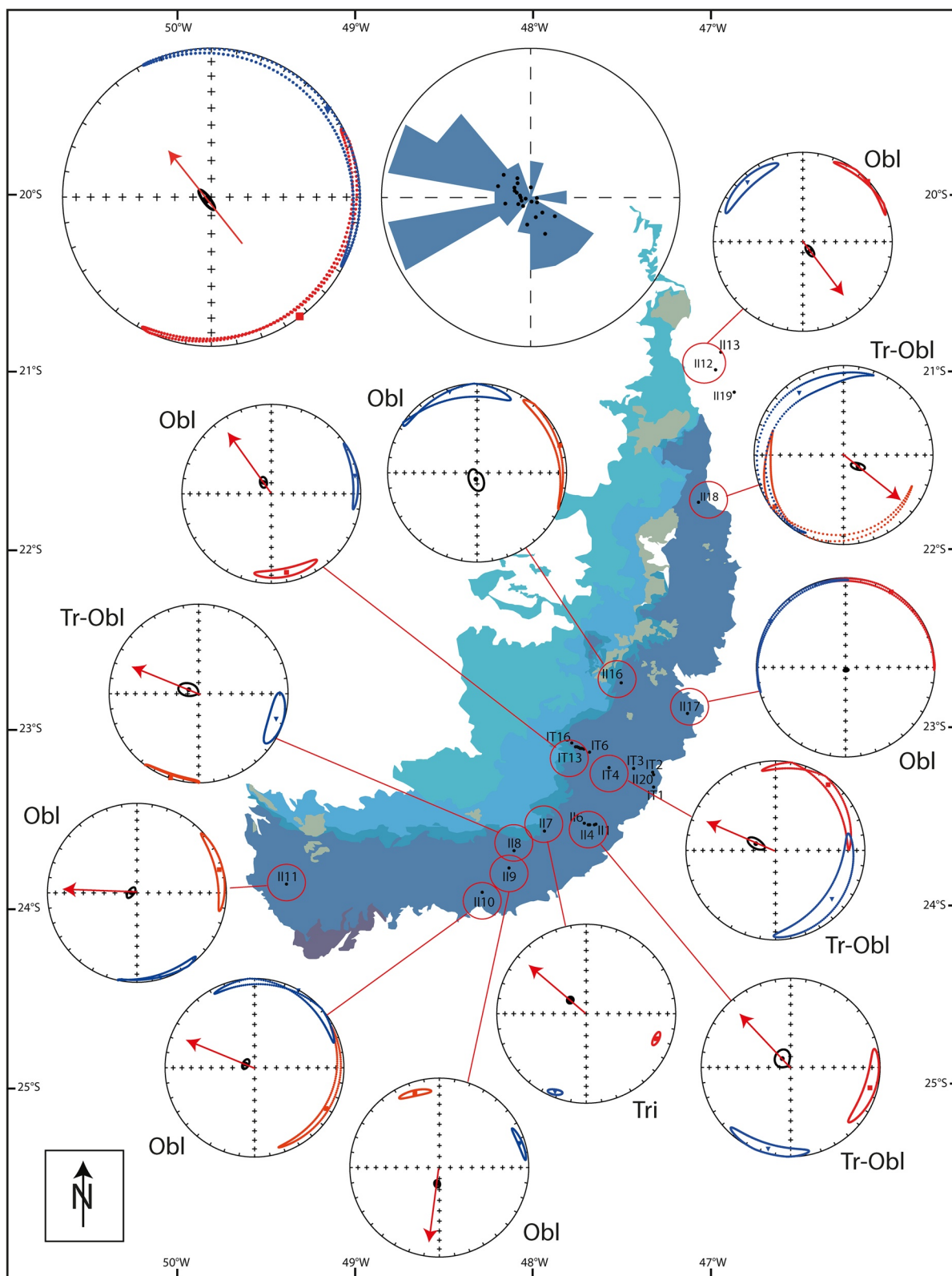
To evaluate the geographic distribution of fabrics, averaging a small number of site-mean fabrics from different lithologies would not result in a representative fabric; however, it is legitimate to average many site-mean fabrics to determine an overall mean for the region. Removing the fabrics of the discordant sites (IT5, II5, and II14), the mean AMS fabric for the Itararé Group rocks can be interpreted as primary depositional, with subvertical  $K_3$  axes and  $K_1$  and  $K_2$  axes distributed in the horizontal plane, with large and overlapping confidence ellipses around their means (Figures 5a, 5b, and 6). Focusing on the distribution of the  $K_3$  axes, these collectively define a prominent NW-SE elongation in the direction of the mean orientation of the  $K_1$  axis (Figures 6 and 7), defining the dominant paleocurrent orientation.

Many site-mean fabrics are subparallel to bedding, and others have more pronounced imbrication but confidence ellipses around the  $K_3$  axes that include the vertical (sites IT1, IT2, IT8, II1, II2, II16, and II20). To evaluate the overall imbrication orientation in greater detail, the  $K_3$  axis-orientation of these seven (7/33) sites was eliminated, and the remainder of site-mean minimum axes plotted on a rose diagram (Figure 7). A dominant distribution to the NW is apparent, with a narrower distribution to the WSW and a smaller distribution to the SE and SSE also present. The distribution to the WSW, however, is made up by relatively small imbrication angles, which may be considered less significant for such analysis, and the more pronounced ~NW-SE trend defines the dominant paleocurrent orientation, with prevalent sediment transport direction to the NW.

## 4.2. Depositional Environments

Taira (1989) conducted an AMS study of natural sedimentary rocks from modern fluvial, eolian dune, and beach environments as well as flume experiments using sediment deposited under different regimes, and supported by photometric quartz  $c$ -axis and microscopic grain counting measurements of thin sections. Four mechanisms of fabric orientation in sedimentary regimes were identified: "gravity" (including





deposition on a slope), “current”, “grain collision”, and “viscous suspension”. Based on two parameters, the  $q$ -value ( $L/F$  of the AMS fabrics and defined as  $(K_1 - K_2)/[0.5(K_1 + K_2) - K_3]$  following Granar [1957]) and  $\beta$ , the imbrication angle of the fabrics relative to the bedding plane, Taira (1989) empirically drew regions on such diagram comprising the values of  $q$  and  $\beta$  that define the four mechanisms. For settling under prevalent gravity and absence of current or turbulence, the  $K_3$  axes align subvertically, while the  $K_1$  and  $K_2$  axes are distributed within the bedding plane, generating oblate susceptibility ellipsoids (Tarling & Hrouda, 1993). The fabrics are strongly foliated (low  $q$ -value) and low imbricated (low  $\beta$ -value). As the slope of the substrate increases, the imbrication angle relative to bedding will increase, whereas  $q$  increases somewhat, but generally maintains low values (Taira, 1989). Current flow causes elongated grains with shape anisotropy to reorient with  $K_1$  axes rotating to parallel to the flow direction. Lift and drag forces flip downcurrent dipping grains so that they become imbricated in the upcurrent direction by tangential shear stresses (Taira, 1989). As the bottom shear stresses increase, the imbrication angle increases up to  $10^\circ$ – $15^\circ$ , and stronger lineations develop, whether parallel to the current or orthogonal intersection lineations, resulting in increased  $q$ -values (Taira, 1989). Grain collision, most commonly results from the layer by layer collision of grains, typically on an inclined surface, and was theoretically investigated by Rees (1968). Sediment grains oriented by such collision typically align with the  $K_1$  axes parallel to the shear stress and imbrication was shown both theoretically and experimentally to increase from  $\sim 20^\circ$  to  $35^\circ$  (Hamilton et al., 1968; Rees, 1968) and the  $q$ -value to be high (0.6–0.7) when compared with gravity fabrics (on horizontal or sloped surfaces) (Taira, 1989). Additionally, particles in non-Newtonian fluids may orient in a viscous fluid, such as magma flows and lava. Despite the limited experimental data available, Rees and Woodall (1975) observed  $q$  and  $\beta$  to be intermediate and between current deposition and grain collision on the  $q$ – $\beta$  diagram, suggesting that a combination of the two mechanisms acts on viscously suspended particles (Taira, 1989). The  $q$ – $\beta$  diagram was successfully applied in a number of recent studies conducted in different environments ranging from gravelly fan delta systems to turbidite sequences (e.g., Park et al., 2013; Tamaki et al., 2015); however, Novak et al. (2014), who applied the method to accretionary prism sediments, further recognized that data often plotted outside the  $q$ – $\beta$  fields defined by Taira (1989). They interpreted data that plot at  $q$ -values intermediate between deposition on slope and grain suspension ( $\sim 0.2 < q < \sim 0.4$ ) as a combination of these two processes. Most importantly, they introduced the field of “deformation/disturbance” for highest  $q$ -values ( $0.7 < q < 1.3$ ) spanning the range of possible  $\beta$  values, and they introduced a “tilting” regime, for high imbrication angles ( $\beta > 40^\circ$ ) that exceed those resulting from natural sedimentary processes, and  $q$ -values  $< 0.7$ . They attribute data plotting in this field to undeformed tilted blocks, which preserve the primary magnetic fabrics, albeit with steeper imbrications (Novak et al., 2014).

The majority of data from this study plot within the “gravity” to “grain collision” areas (Figure 8). Despite the scatter of the individual specimen data, the distribution of the site-mean data is remarkably aligned within the fields outlined for the different depositional regimes, with just two site means (sandstone site IT11 and diamictite site II6) plotting just outside the “current” and “viscous suspension” areas, and between deposition on a slope and grain suspension, possibly representing somewhat higher sediment concentrations in a flow or deposition on a slope. As would be expected, the scatter of the individual specimen data for each site increases as the site-mean data plot farther from the main distribution, as can be appreciated from visually inspecting the  $q$ – $\beta$  diagram (Figure 8). Notably, the slumped sediments at site IT5 plot in the deformation/disturbance field of Novak et al. (2014), with data in geographic and stratigraphic specimen coordinates spanning a range of imbrication angles, as already shown in Figure 6. This evidence supports the interpretation of a composite fabric that was generated by the slumping of a wet sediment, with a prominent intersection lineation, and subsequent gravitational/compactional reorientation of grains that realigned the  $K_3$  axes to subvertical.

At a glance, the finer grained lithologies with  $\sim$ bedding parallel fabrics, the claystones and rhythmites, plot at the intersection of the “gravity” and “current” areas of the diagram, consistently with expectations. At the opposite end, the coarsest sandstones at sites II8 and IT8, and the turbidite at site IT4 plot in the “grain

**Figure 7.** Representative site-mean AMS fabrics for the Itararé Group plotted on lower hemisphere stereonet with 95% confidence ellipses around the anisotropy principal axes (red squares, blue triangles, and black circles are  $K_1$ ,  $K_2$ , and  $K_3$ , respectively). The larger stereonet represents the mean Itararé Group fabric (symbols as above), revealing a prominent elongation of the  $K_3$  axes (red arrow). The rose diagram depicts the distribution of the site-mean  $K_3$  axes for all sites with  $K_3$  axes distinct from vertical at the 95% confidence level (26/33), see text for details, and indicating a prevalent direction of imbrication to the NW, representing the dominant paleocurrent and sediment transport direction for the Itararé Group rocks.

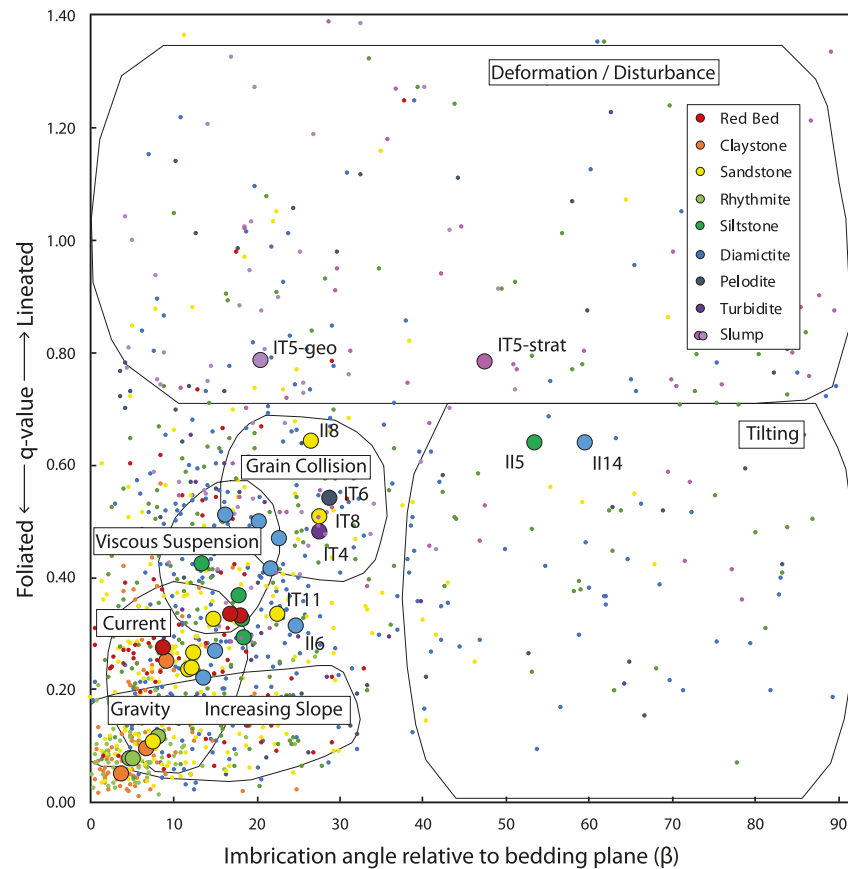


**Figure 8.**  $q$ - $\beta$  plot of Taira (1989).  $q$ -Values (magnetic lineation over magnetic foliation) versus the imbrication angle relative to the bedding plane ( $\beta$ ) for data at the specimen level (small symbols) and site-mean level (large symbols) color coded by lithology, see legend. The areas drawn within the plot define the values of  $q$ - $\beta$  empirically determined by Taira (1989) and Novak et al. (2014) for different depositional and deformation mechanisms (see text for details). With the exception of a few sites, the majority of site-mean data plot within the depositional regimes outlined by Taira (1989), note also that the dispersion of the data increases away from the origin of the plot (see text for details).

collision” area, as expected for the highest-energy deposits. The pelodite at site IT6 also plots in this field: pelodites are formed by redeposition of the finer grain size fraction of diamictites after being removed by water action (Harland et al., 1966; Woodworth, 1912). While massive, and void of sedimentary structures, the strong lineation at IT6 ( $q$ -value = 0.53), perpendicular to the elongation direction of the  $K_3$  axes (Figure 6f), is interpreted here as an intersection lineation of phyllosilicate mineral planes resting at varying angles around the mean imbrication and is consistent with a massive deposit resulting from reworking by strong currents. Most sandstones, siltstones, and the red bed sites plot at the intersection of the “current” and “viscous suspension” areas of the plot, whereas the diamictites extend from the “current” area to the “viscous suspension/grain collision” areas. Additionally, the siltstone at site II5 and the diamictite at site II14, that were already interpreted as carrying secondary magnetic fabrics, plot in the “tilting” region of (2014). The beds collected were flat-lying and otherwise undisturbed, therefore, despite the dominant paramagnetic behavior for these sites at room temperature (cf., Figures 3 and 4), the fabrics and their imbrication are attributed to authigenic grains precipitated from hydrothermal fluids migrating during the remagnetization events described by Bilardello et al. (2018) and do not reflect primary sedimentary fabrics.

The Itararé Group rocks have been widely interpreted as fining upwards glacial–subglacial successions representing sea-level rise during glacial melting (e.g., França & Potter, 1988, 1991; Limarino & Spalletti, 2006; Rocha-Campos et al., 2008; Santos et al., 1996). Distal facies, such as rhythmites and shales, result from suspension or suspension plus traction. Mass transport may develop into gravitational flows, segregating sand out of the main flow, and depositing sandy debris and occasional turbidites (França & Vesely, 2007; Vesely

et al., 2018). More specifically, in a more proximal to distal setting relative to the source glaciers, the poorly to well-sorted sandstones, often aggradational and with rapid vertical facies changes, have been interpreted as subaqueous outwash-fan apron deposits, grading laterally into diamictites and mudstones (Carvalho & Vesely, 2017; França & Vesely, 2007; Mottin et al., 2018). The abundant massive and unsorted diamictites represent subaqueous mass transport deposits resulting from resedimentation of glacially derived debris and previously accumulated sediments and more distally can involve slumping (Arab et al., 2009; Mottin et al., 2018). Rhythmite and sandstone sequences represent deposition under hydrodynamic underflows associated with suspension fallout and sediment traction. Coarsening upward trends are attributed to progradation, ascribing some rhythmite units to tide-influenced delta front regions (Mottin et al., 2018). Delta front facies evolve into tide-influenced delta-plain deposits consisting of medium to coarse sandstones, often channelized and lenticular, with subordinate thin and massive mudstones and sandstones. Shale deposits represent the most distal environments characterized by sediment suspension (Carvalho & Vesely, 2017; França & Vesely, 2007; Mottin et al., 2018).

The depositional environments interpreted for the different facies of the Itararé Group rocks are generally consistent with the depositional regimes extrapolated from the  $q$ - $\beta$  diagram, with claystones and rhythmites deposited under the least influence of currents, and flow conditions increasing for most sandstone and siltstone deposits, and evolving into mass transport viscous suspension and grain collision regimes for most of the diamictites and the turbidite deposit. The sandstone deposits at II8 and IT8, a buff sand deposited as a thin (~40 cm) layer and a medium sand deposit, respectively, fit the description of outwash deposits associated with the turbidites and diamictites. The agreement between the stratigraphic interpretations and the  $q$ - $\beta$  diagram thus confirms the interpretation of primary AMS fabrics, with the exception of sites IT5, II5, and II14. This interpretation in turn validates the use of AMS to determine paleocurrent directions, indicating a dominant NW transport direction across the state of São Paulo.

#### 4.3. Independent Evidence for Transport Direction

Many studies have investigated the ice-transport direction of the Itararé Group rocks and were nicely summarized by Gesicki et al. (2002) and da Rosa et al. (2016). These consist of direct evidence derived from landforms and striations arising from glacier movement, and specific to the state of São Paulo, eight such occurrences have been reported. Three studies (Almeida, 1948; Amaral, 1965; Viviani & Rocha-Campos, 2002) investigated streamlined landforms, *roches moutonnées* and whalebacks, with superimposed striations indicating paleo-ice flow to the northwest. A streamlined elongated granitic body studied by Rocha-Campos et al. (1968) possessed SE-NW-oriented striated surfaces. A study by Caetano-Chang et al. (1990) describe soft-sediment grooved surfaces of subglacial origin on a diamictite deposit, where striations terminating in lodged pebbles indicate a paleo-ice-flow direction to the NW. Pérez-Aguilar et al. (2009) describe striated pavements on Precambrian granites oriented to the NW and displaying crescentic fractures and gouges that indicate a northwestward ice flow. The two surfaces described are covered by diamictites interpreted to be deposited by an active glacier moving over the bed. Other evidence comes from studies of striated clast pavements at two different localities by Rocha-Campos et al. (1968, 1969, 1976) and consisting of linear concentrations of clasts of different sizes within the same stratigraphic horizon, where the clasts are often flat and contain parallel striations with uniform orientations. At the first locality, the pavement is within diamictites, interpreted as subglacial tillites, displaying faceted clasts with striated upper surfaces. From these, a paleo-ice flow to the northwest was interpreted based on clast imbrication and on the presence of crescentic fractures in a granitic boulder contained within the pavement. At the second locality, two pavements possessing faceted clasts with striated top surfaces were identified. Based on clast imbrication, the direction of paleo-ice flow was interpreted to be N-NW.

Paleocurrent directions have also been determined from sparse sedimentary structures within sandstone deposits from the same region (Arab et al., 2009), indicating WNW to NNW sediment transport directions. The paleocurrent and paleo-ice-flow directions obtained from these independent methods, thus appear to be related, and agree nicely with the AMS lineation data reported here for the entire state of São Paulo. Such correlations thus fully support the inferred regional paleocurrent direction to the NW, which is intrinsically tied to ice-kinematics. Following multiple lines of evidence, this study confirms the validity of the AMS



method to aid recognition of the depositional environments and the current directions for sediments of glacial affinity that are mostly void of sedimentary structures.

## 5. Conclusions

We conducted an AMS study on specimens collected from 33 sedimentary rocks sites within the Itararé Group throughout the entire state of São Paulo, Brazil. The rocks were deposited during the LPIA and do not display macroscopic sedimentary structures or ice-kinematic indicators.

Low-temperature magnetic experiments (DC magnetic remanence and AC magnetic susceptibility) reveal a complex magnetic mineralogy for the different sites, consisting of assemblages of magnetite plus goethite, or magnetite and hematite plus goethite, with magnetite and hematite sometimes occurring as nanophases. However, room temperature magnetic hysteresis data and AC in-phase susceptibility between 10 K and room temperature indicate that at room temperature the dominant susceptibility response is paramagnetic.

The paramagnetic susceptibility response at room temperature implies that AMS is largely carried by the paramagnetic component and records primary depositional fabrics. The majority of site-mean AMS data are triaxial-oblate with bedding parallel to slightly imbricated ellipsoids. The site-mean magnetic lineations are subhorizontal, girdled NE-SW. The site-mean minimum axes are subvertical and distributed along a SE-NW elongation direction, with prominent imbrication to the NW. Together, the orientation of the magnetic lineation and orientation of the site-mean AMS fabrics suggest deposition in a current with a dominant direction of transport to the NW.

Evaluation of the AMS data on a  $q$ - $\beta$  diagram confirms that the Itararé Group sedimentary rocks were deposited under varying conditions ranging from gravitational settling to increasing current conditions, evolving into mass transport processes involving grain collision. These results agree with the depositional environments interpreted for the Itararé Group rocks around the Paraná Basin, lending support to our magnetic fabric interpretation. We emphasize the validity of the  $q$ - $\beta$  diagram, which is rather underutilized in sedimentary fabric studies.

Ice-flow kinematics within the state of São Paulo, as determined from rare direct field evidence obtained at a limited number of localities, supports the SE-NW paleocurrent directions obtained here across the entire state, confirming our interpreted direction of sediment transport to the NW.

Our results confirm the validity of AMS as a rapid, nondestructive technique to investigate magnetic fabrics and assess depositional regimes in sedimentary rocks, allowing determination of paleocurrent directions where direct evidence is otherwise scarce.

## Acknowledgments

Irene Raposo is thanked for all aspects of the field component of this work and use of the lab at the University of São Paulo, Brazil, for the anisotropy of magnetic susceptibility measurements for the sites labeled IT, with funding by the São Paulo Research Foundation (FAPESP) grant 2011/51204-0. I am indebted to William Callebort for performing the majority of the magnetic anisotropy measurements at the Institute for Rock Magnetism (IRM), University of Minnesota, with funding by the National Science Foundation grants NSF/EAR 1028690 and 1339505, and additional support by the University of Minnesota's Undergraduate Research Opportunity Program. The IRM is a US National multiuser facility supported through the Instrumentation and Facilities program of the National Science Foundation, Earth Sciences Division, and by funding from the University of Minnesota. This is IRM publication #2102.

## Data Availability Statement

All data used for this publication can be accessed through the public domain Data Repository for the University of Minnesota (DRUM) (at <https://doi.org/10.13020/jjdx-1m95>).

## References

- Abbott, D. H., & Isley, A. E. (2002). The intensity, occurrence, and duration of superplume events and eras over geological time. *Journal of Geodynamics*, 34(2), 265–307. [https://doi.org/10.1016/S0264-3707\(02\)00024-8](https://doi.org/10.1016/S0264-3707(02)00024-8)
- Almeida, F. F. M. (1948). A “Roche Moutonnée” de Salto, Estado de São Paulo. *Boletim Geologia e Metalurgia*, 5, 112–118.
- Amaral, S. E. (1965). Nova ocorrência de rocha moutonnée em Salto, SP. *Boletim da Sociedade Brasileira de Geologia*, 14, 71–82.
- Arab, P. B., Perinotto, J. A. J., & Assine, M. L. (2009). Grupo itararé (P - C da bacia do Paraná) nas regiões de Limeira e Piracicaba - SP: Contribuição ao estudo das litofácies. *Geociências*, 28(4), 501–521.
- Araújo, C. C., Yamamoto, J. K., Rostirolla, S. P., Madrucci, V., & Tankard, A. (2005). Tar sandstones in the Paraná Basin of Brazil: Structural and magmatic controls of hydrocarbon charge. *Marine and Petroleum Geology*, 22(5), 671–685. <https://doi.org/10.1016/j.marpetgeo.2005.01.006>
- Araújo, L. M., Triguês, J. A., Cerqueira, J. R., & Freitas, L. C. D. S. (2000). The atypical Permian petroleum system of the Paraná Basin, Brazil. *AAPG Memoir*, 73, 377–402. <https://doi.org/10.1306/m73705c26>
- Balsley, J. R., & Buddington, A. F. (1960). Magnetic susceptibility anisotropy and fabric of some Adirondack granites and orthogneisses. *American Journal of Science*, 258A, 6–20.

- Bangert, B., Stollhofen, H., Lorenz, V., & Armstrong, R. (1999). The geochronology and significance of ash-fall tuffs in the glaciogenic Carboniferous-Permian Dwyka Group of Namibia and South Africa. *Journal of African Earth Sciences*, 29, 33–49. [https://doi.org/10.1016/S0899-5362\(99\)00078-0](https://doi.org/10.1016/S0899-5362(99)00078-0)
- Biedermann, A. (2018). Magnetic anisotropy in single crystals: A review. *Geosciences*, 8(8), 302. <https://doi.org/10.3390/geosciences8080302>
- Bilardello, D. (2016). *Magnetic anisotropy: Theory, instrumentation, and techniques. Reference module in Earth systems and environmental sciences*. Amsterdam, The Netherlands: Elsevier Inc. <https://doi.org/10.1016/B978-0-12-409548-9.09516-6>
- Bilardello, D., Callebert, W. C., & Davis, J. R. (2018). Evidence for widespread remagnetizations in South America, case study of the Itararé Group rocks from the state of São Paulo, Brazil. *Frontiers of Earth Science*, 6, 1–25. <https://doi.org/10.3389/feart.2018.00182>
- Bilardello, D., & Kodama, K. P. (2009). Measuring remanence anisotropy of hematite in red beds: Anisotropy of high-field isothermal remanence magnetization (hf-AIR). *Geophysical Journal International*, 178(3), 1260–1272. <https://doi.org/10.1111/j.1365-246X.2009.04231.x>
- Borradaile, G. J., & Lagroix, F. (2000). Thermal enhancement of magnetic fabrics in high grade gneisses. *Geophysical Research Letters*, 27(16), 2413–2416. <https://doi.org/10.1029/2000GL008522>
- Borradaile, G. J., & Werner, T. (1994). Magnetic anisotropy of some phyllosilicates. *Tectonophysics*, 235(3), 223–248. [https://doi.org/10.1016/0040-1951\(94\)90196-1](https://doi.org/10.1016/0040-1951(94)90196-1)
- Caetano-Chang, M. R., Oliveira, J. P. D., & Brighetti, J. M. P. (1990). Pavimento Estriado Em Rochas Do Subgrupo Itararé Ao Longo Do Rio Piritubinha, Sul Do Estado De São Paulo. *Revista Brasileira de Geociências*, 20, 333–335. <https://doi.org/10.25249/0375-7536.1990333335>
- Carter-Stiglitz, B., Moskowitz, B., & Jackson, M. (2001). Unmixing magnetic assemblages and the magnetic behavior of bimodal mixtures. *Journal of Geophysical Research*, 106(B11), 26397–26411.
- Carvalho, A. H., & Vesely, F. F. (2017). Facies relationships recorded in a Late Paleozoic fluvio-deltaic system (Paraná Basin, Brazil): Insights into the timing and triggers of subaqueous sediment gravity flows. *Sedimentary Geology*, 352, 45–62. <https://doi.org/10.1016/j.sedgeo.2016.12.004>
- da Rosa, E. L. M., Vesely, F. F., & França, A. B. (2016). A review on late Paleozoic ice-related erosional landforms in the Paraná Basin: Origin and paleogeographical implications. *Brazilian Journal of Geology*, 46(2), 147–166. <https://doi.org/10.1590/2317-4889201620160050>
- Ernesto, M., Raposo, M. I. B., Marques, L. S., Renne, P. R., Diogo, L. A., & de Min, A. (1999). Paleomagnetism, geochemistry and dating of the North-eastern Paraná Magmatic Province: Tectonic implications. *Journal of Geodynamics*, 28(4–5), 321–340. [https://doi.org/10.1016/S0264-3707\(99\)00013-7](https://doi.org/10.1016/S0264-3707(99)00013-7)
- Fedorchuk, N. D., Isbell, J. L., Griffis, N. P., Montañez, I. P., Vesely, F. F., Iannuzzi, R., et al. (2019). Origin of paleovalleys on the Rio Grande do Sul Shield (Brazil): Implications for the extent of late Paleozoic glaciation in west-central Gondwana. *Palaeogeography, Palaeoclimatology, Palaeoecology*, 531, 108738. <https://doi.org/10.1016/j.palaeo.2018.04.013>
- Flinn, D. (1978). Construction and computation of three-dimensional progressive deformations. *Journal of the Geological Society*, 135(3), 291–305. <https://doi.org/10.1144/gsjgs.135.3.0291>
- França, A. B., & Potter, P. E. (1988). Estratigrafia, ambiente deposicional e análise de reservatório do Grupo Itararé (Permocarbonífero), Bacia do Paraná (parte 1). *Boletim de Geociências da Petrobrás*, 2, 147–191.
- França, A. B., & Potter, P. E. (1991). Stratigraphy and reservoir potential of glacial deposits of the Itararé Group (Carboniferous-Permian), Paraná Basin, Brazil. *American Association of Petroleum Geologists Bulletin*, 75, 62–85.
- França, A. B., & Vesely, F. F. (2007). Stratigraphy and sedimentology of the Late Paleozoic glacial record of the Paraná Basin: Brazil Almério Bar. In *I Workshop—Problems in Western Gondwana Geology*. (pp. 46–54).
- Franco, D. R., Ernesto, M., Ponte-Neto, C. F., Hinnov, L. A., Berquó, T. S., Fabris, J. D., & Rosière, C. A. (2012). Magnetostratigraphy and mid-palaeolatitude VGP dispersion during the Permo-Carboniferous Superchron: Results from Paraná Basin (Southern Brazil) rhythmites. *Geophysical Journal International*, 191(3), 993–1014. <https://doi.org/10.1111/j.1365-246X.2012.05670.x>
- Gesicki, A. L. D., Riccomini, C., & Boggiani, P. C. (2002). Ice flow direction during late Paleozoic glaciation in western Paraná Basin, Brazil. *Journal of South American Earth Sciences*, 14(8), 933–939. [https://doi.org/10.1016/S0895-9811\(01\)00076-1](https://doi.org/10.1016/S0895-9811(01)00076-1)
- Gesicki, A. L. D., Riccomini, C., Boggiani, P. C., & Coimbra, A. M. (1998). The Aquidauana Formation (Parana Basin) in the context of the late Paleozoic glaciation in western Gondwana. *Journal of African Earth Sciences*, 27, 81–82.
- Granar, L. (1957). Magnetic measurements on Swedish varved sediments. *Arkiv för Geofysik*, 3, 1–40.
- Guerrero-Suarez, S., & Martín-Hernández, F. (2012). Magnetic anisotropy of hematite natural crystals: Increasing low-field strength experiments. *International Journal of Earth Sciences*, 101(3), 625–636. <https://doi.org/10.1007/s00531-011-0666-y>
- Guyodo, Y., LaPara, T. M., Anschutz, A. J., Penn, R. L., Banerjee, S. K., Geiss, C. E., & Zanner, W. (2006). Rock magnetic, chemical and bacterial community analysis of a modern soil from Nebraska. *Earth and Planetary Science Letters*, 251(1–2), 168–178. <https://doi.org/10.1016/j.epsl.2006.09.005>
- Hamilton, N., Owens, W. H., & Rees, A. I. (1968). Laboratory experiments on the production of grain orientation in shearing sand. *The Journal of Geology*, 76(4), 465–472. <https://doi.org/10.1086/627344>
- Harland, W. B., Herod, K. N., & Krinsley, D. H. (1966). The definition and identification of tills and tillites. *Earth-Science Reviews*, 2(C), 225–256. [https://doi.org/10.1016/0012-8252\(66\)90030-4](https://doi.org/10.1016/0012-8252(66)90030-4)
- Henry, B., Jordanova, D., Jordanova, N., Souque, C., & Robion, P. (2003). Anisotropy of magnetic susceptibility of heated rocks. *Tectonophysics*, 366(3–4), 241–258. [https://doi.org/10.1016/S0040-1951\(03\)00099-4](https://doi.org/10.1016/S0040-1951(03)00099-4)
- Holz, M., França, A. B., Souza, P. A., Iannuzzi, R., & Rohn, R. (2010). A stratigraphic chart of the Late Carboniferous/Permian succession of the eastern border of the Paraná Basin, Brazil, South America. *Journal of South American Earth Sciences*, 29(2), 381–399. <https://doi.org/10.1016/j.jsames.2009.04.004>
- Housen, B. A., Richter, C., & van der Pluijm, B. A. (1993). Composite magnetic anisotropy fabrics: Experiments, numerical models and implications for the quantification of rock fabrics. *Tectonophysics*, 220(1–4), 1–12. [https://doi.org/10.1016/0040-1951\(93\)90219-A](https://doi.org/10.1016/0040-1951(93)90219-A)
- Hrouda, F. (2002). Low-field variation of magnetic susceptibility and its effect on the anisotropy of magnetic susceptibility of rocks. *Geophysical Journal International*, 150(3), 715–723. <https://doi.org/10.1046/j.1365-246X.2002.01731.x>
- Isbell, J. L., Miller, M. F., Wolfe, K. L., & Lenaker, P. A. (2003). Timing of late Paleozoic glaciation in Gondwana: Was glaciation responsible for the development of northern hemisphere cyclotheams? *Special Paper of the Geological Society of America*, 370, 5–24. <https://doi.org/10.1130/0-8137-2370-1.5>
- Jackson, M., & Tauxe, L. (1991). Anisotropy of magnetic susceptibility and remanence: Developments in the characterization of tectonic, sedimentary and igneous fabric. *Reviews of Geophysics*, 29(S1), 371–376. <https://doi.org/10.1002/rog.1991.29.s1.371>
- Jelinek, V. (1981). Characterization of the magnetic fabric of rocks. *Tectonophysics*, 79, 63–67. [https://doi.org/10.1016/0040-1951\(81\)90110-4](https://doi.org/10.1016/0040-1951(81)90110-4)
- Kodama, K. P. (2012). *Paleomagnetism of sedimentary rocks*. Chichester, UK: John Wiley & Sons, Ltd. <https://doi.org/10.1002/9781118384138>
- Lagroix, F., & Borradaile, G. J. (2000). Magnetic fabric interpretation complicated by inclusions in mafic silicates. *Tectonophysics*, 325(3–4), 207–225. [https://doi.org/10.1016/S0040-1951\(00\)00125-6](https://doi.org/10.1016/S0040-1951(00)00125-6)

- Li, Y.-X., & Kodama, K. P. (2005). Assessing thermal effects on magnetic fabrics of sedimentary rocks: Results from synthetic and natural samples. *Geophysical Research Letters*, 32, L04314. <https://doi.org/10.1029/2004GL022049>
- Limarino, C. O., & Spalletti, L. A. (2006). Paleogeography of the upper Paleozoic basins of southern South America: An overview. *Journal of South American Earth Sciences*, 22(3–4), 134–155. <https://doi.org/10.1016/j.jsames.2006.09.011>
- Martin-Hernandez, F., & Guerrero-Suarez, S. (2012). Magnetic anisotropy of hematite natural crystals: High field experiments. *International Journal of Earth Sciences*, 101(3), 637–647. <https://doi.org/10.1007/s00531-011-0665-z>
- Martin-Hernández, F., & Hirt, A. M. (2003). The anisotropy of magnetic susceptibility in biotite, muscovite and chlorite single crystals. *Tectonophysics*, 367(1–2), 13–28. [https://doi.org/10.1016/S0040-1951\(03\)00127-6](https://doi.org/10.1016/S0040-1951(03)00127-6)
- Martin-Hernández, F., Lüneburg, C. M., Aubourg, C., & Jackson, M. (2004). Magnetic fabric: Methods and applications—An introduction. *Geological Society, London, Special Publications*, 238(1), 1–7. <https://doi.org/10.1144/GSL.SP.2004.238.01.01>
- Matos, S. L. F., Yamamoto, J. K., Riccomini, C., Hachiro, J., & Tassinari, C. C. G. (2001). Absolute dating of Permian ash-fall in the Rio Bonito formation, Paraná Basin, Brazil. *Gondwana Research*, 4(3), 421–426. [https://doi.org/10.1016/S1342-937X\(05\)70341-5](https://doi.org/10.1016/S1342-937X(05)70341-5)
- Menezes, P. T. L., & Travassos, J. M. (2000). A scalar audiomagnetotelluric survey across an outcropping dike. *Pure and Applied Geophysics*, 157(9), 1493–1507. <https://doi.org/10.1007/PL00001130>
- Milani, E. J., Faccini, U. F., Scherer, C. M., Araújo, L. M., & Cupertino, J. A. (1998). Sequências e hierarquia estratigráfica da bacia do Paraná (Ordoviciano ao Cretáceo), sul do Brasil. *Boletim IG-USP: Serie Científica*, 29, 125–173.
- Milani, E. J., França, A. B., & Schneider, R. L. (1994). Bacia do Paraná. *Boletim de Geociências da Petrobrás*, 8, 69–82.
- Milani, E. J., & Zalán, P. V. (1999). An outline of the geology and petroleum systems of the Paleozoic interior basins of South America. *Episodes*, 22, 199–205.
- Mottin, T. E., Vesely, F. F., de Lima Rodrigues, M. C. N., Kipper, F., & de Souza, P. A. (2018). The paths and timing of late Paleozoic ice revisited: New stratigraphic and paleo-ice flow interpretations from a glacial succession in the upper Itararé Group (Paraná Basin, Brazil). *Palaeogeography, Palaeoclimatology, Palaeoecology*, 490, 488–504. <https://doi.org/10.1016/j.palaeo.2017.11.031>
- Novak, B., Housen, B., Kitamura, Y., Kanamatsu, T., & Kawamura, K. (2014). Magnetic fabric analyses as a method for determining sediment transport and deposition in deep sea sediments. *Marine Geology*, 356, 19–30. <https://doi.org/10.1016/j.margeo.2013.12.001>
- Özdemir, Ö., & Dunlop, D. J. (2010). Hallmarks of maghemitization in low-temperature remanence cycling of partially oxidized magnetite nanoparticles. *Journal of Geophysical Research*, 115, B02101. <https://doi.org/10.1029/2009JB006756>
- Parés, J. M., & van der Pluijm, B. A. (2002). Phyllosilicate fabric characterization by Low-Temperature Anisotropy of Magnetic Susceptibility (LT-AMS). *Geophysical Research Letters*, 29(24), 2215. <https://doi.org/10.1029/2002GL015459>
- Park, M. E., Cho, H., Son, M., & Sohn, Y. K. (2013). Depositional processes, paleoflow patterns, and evolution of a Miocene gravelly fan-delta system in SE Korea constrained by anisotropy of magnetic susceptibility analysis of interbedded mudrocks. *Marine and Petroleum Geology*, 48, 206–223. <https://doi.org/10.1016/j.marpetgeo.2013.08.015>
- Pérez-Aguilar, A., Petri, S., Hypólito, R., Ezaki, S., de Souza, P. A., Juliani, C., et al. (2009). Superfícies estriadas no embasamento granítico e vestígio de pavimento de clastos neopaleozóicos na região de Salto, SP. *Revista Escola de Minas*, 62(1), 17–22. <https://doi.org/10.1590/s0370-44672009000100004>
- Raposo, M. I. B., Esteves, M. C. B., & dos Santos, P. R. (2021). Can magnetic fabric indicate the direction of a glacier movement? An example from Itararé Group and Aquidauana Formation, Paraná Basin, Brazil. *Journal of South American Earth Sciences*, 106, 103003. <https://doi.org/10.1016/j.jsames.2020.103003>
- Rees, A. I. (1968). The production of preferred orientation in a concentrated dispersion of elongated and flattened grains. *The Journal of Geology*, 76(4), 457–465.
- Rees, A. I., & Woodall, W. A. (1975). The magnetic fabric of some laboratory-deposited sediments. *Earth and Planetary Science Letters*, 25(2), 121–130. [https://doi.org/10.1016/0012-821X\(75\)90188-0](https://doi.org/10.1016/0012-821X(75)90188-0)
- Roberts, A. P., Zhao, X., Heslop, D., Abrajevitch, A., Chen, Y.-H., Hu, P., et al. (2020). Hematite ( $\alpha\text{-Fe}_2\text{O}_3$ ) quantification in sedimentary magnetism: Limitations of existing proxies and ways forward. *Geoscience Letters*, 7(1), 8. <https://doi.org/10.1186/s40562-020-00157-5>
- Rocha-Campos, A. C., Canuto, J. R., & dos Santos, P. R. (2000). Late Paleozoic glaciotectionic structures in northern Paraná Basin, Brazil. *Sedimentary Geology*, 130(1–2), 131–143. [https://doi.org/10.1016/S0037-0738\(99\)00110-4](https://doi.org/10.1016/S0037-0738(99)00110-4)
- Rocha-Campos, A. C., De Oliveira, M. E. C. B., Santos, P. R., & Saad, A. R. (1976). Boulder pavements and the sense of movement of late Paleozoic glaciers in central eastern São Paulo State, Parana Basin, Brazil. *Boletim IG*, 7, 149–160. <https://doi.org/10.11606/issn.2316-8978.v7i0p149-160>
- Rocha-Campos, A. C., dos Santos, P. R., & Canuto, J. R. (2008). Late Paleozoic glacial deposits of Brazil: Paraná Basin. In *Special Paper 441: Resolving the Late Paleozoic Ice Age in time and space* (Vol. 441, pp. 97–114). Boulder, CO: Geological Society of America. [https://doi.org/10.1130/2008.2441\(07\)](https://doi.org/10.1130/2008.2441(07))
- Rocha-Campos, A. C., Farjallat, J. E., & Yoshida, R. (1968). New glacial features of the Upper Paleozoic Itararé Subgroup in the State of São Paulo, Brazil. *Boletim da Sociedade Brasileira de Geologia*, 17, 47–57.
- Rocha-Campos, A. C., Farjallat, J. E. S., & Yoshida, R. (1969). Crescentic marks on a Late Paleozoic glacial pavement in southeastern Brazil. *Geological Society of America Bulletin*, 80, 1123–1126.
- Rosa, E. L. M., Vesely, F. F., Isbell, J. L., Kipper, F., Fedorchuk, N. D., & Souza, P. A. (2019). Constraining the timing, kinematics and cyclicity of Mississippian-Early Pennsylvanian glaciations in the Paraná Basin, Brazil. *Sedimentary Geology*, 384, 29–49. <https://doi.org/10.1016/j.sedgeo.2019.03.001>
- Santos, P. R., Rocha-Campos, A. C., & Canuto, J. R. (1996). Patterns of late Palaeozoic deglaciation in the Parana Basin, Brazil. *Palaeogeography, Palaeoclimatology, Palaeoecology*, 125(1–4), 165–184. [https://doi.org/10.1016/S0031-0182\(96\)00029-6](https://doi.org/10.1016/S0031-0182(96)00029-6)
- Scotese, C. R., Boucot, A. J., & Mckerrow, W. S. (1999). Gondwanan palaeogeography and palaeoclimatology. *Journal of African Earth Sciences*, 28(1), 99–114. [https://doi.org/10.1016/S0899-5362\(98\)00084-0](https://doi.org/10.1016/S0899-5362(98)00084-0)
- Smirnov, A. V., & Tarduno, J. A. (2000). Low-temperature magnetic properties of pelagic sediments (Ocean Drilling Program Site 805C): Tracers of maghemitization and magnetic mineral reduction. *Journal of Geophysical Research*, 105(B7), 16457–16471. <https://doi.org/10.1029/2000JB900140>
- Souza, P. A. (2006). Late Carboniferous palynostratigraphy of the Itararé Subgroup, northeastern Paraná Basin, Brazil. *Review of Palaeobotany and Palynology*, 138(1), 9–29. <https://doi.org/10.1016/j.revpalbo.2005.09.004>
- Stacey, F. D., Joplin, G., & Lindsay, J. (1960). Magnetic anisotropy and fabric of some foliated rocks from S.E. Australia. *Geofísica Pura e Aplicata*, 47, 30–40. <https://doi.org/10.1007/bf01992481>
- Taira, A. (1989). Magnetic fabrics and depositional processes. In A. Taira & F. Masuda (Eds.), *Sedimentary facies in the active plate margin* (pp. 43–77). Tokyo, Japan: Terra Scientific Publishing Company (TERRAPUB). Retrieved from <http://www.terrapub.co.jp/e-library/taira/pdf/043.pdf>

- Tamaki, M., Suzuki, K., & Fujii, T. (2015). Paleocurrent analysis of Pleistocene turbidite sediments in the forearc basin inferred from anisotropy of magnetic susceptibility and paleomagnetic data at the gas hydrate production test site in the eastern Nankai Trough. *Marine and Petroleum Geology*, 66, 404–417. <https://doi.org/10.1016/j.marpetgeo.2015.02.030>
- Tarling, D. H., & Hrouda, F. (1993). *The magnetic anisotropy of rocks* (217 pp.). London: Chapman and Hall.
- Tauxe, L., Mullender, T. A. T., & Pick, T. (1996). Potbellies, wasp-waists, and superparamagnetism in magnetic hysteresis. *Journal of Geophysical Research*, 101(B1), 571–583.
- Tauxe, L., Shaar, R., Jonestrask, L., Swanson-Hysell, N. L., Minnett, R., Koppers, A. A. P., et al. (2016). PmagPy: Software package for paleomagnetic data analysis and a bridge to the Magnetism Information Consortium (MagIC) Database. *Geochemistry, Geophysics, Geosystems*, 17, 2450–2463. <https://doi.org/10.1002/2016GC006307>
- Thomaz Filho, A., Mizusaki, A. M. P., & Antonioli, L. (2008). Magmatism and petroleum exploration in the Brazilian Paleozoic basins. *Marine and Petroleum Geology*, 25(2), 143–151. <https://doi.org/10.1016/j.marpetgeo.2007.07.006>
- Vesely, F. F., Rodrigues, M. C. N. L., da Rosa, E. L. M., Amato, J. A., Trzaskos, B., Isbell, J. L., & Fedorchuk, N. D. (2018). Recurrent emplacement of non-glacial diamictite during the Late Paleozoic Ice Age. *Geology*, 46(7), 615–618. <https://doi.org/10.1130/G45011.1>
- Viviani, J. B., & Rocha-Campos, A. C. (2002). Late Paleozoic exhumed glacial erosive landscape in Salto, SP. *Anais Da Academia Brasileira de Ciências*, 74, 549–550.
- Weil, A. B., & Yonkee, A. (2009). Anisotropy of magnetic susceptibility in weakly deformed red beds from the Wyoming salient, Sevier thrust belt: Relations to layer-parallel shortening and orogenic curvature. *Lithosphere*, 1(4), 235–256. <https://doi.org/10.1130/L42.1>
- Woodworth, J. B. (1912). Boulder beds of the Caney shales at Talihina, Oklahoma. *The Geological Society of America Bulletin*, 23, 457–462.